The University of Osaka
Institutional Knowledge Archive

Title	Interaction between Carbon and Extended Defects in Fe Studied by First-Principles Based Interatomic Potential
Author(s)	Pham Thi, Dung
Citation	大阪大学, 2022, 博士論文
Version Type	VoR
URL	https://doi.org/10.18910/88030
rights	
Note	

The University of Osaka Institutional Knowledge Archive : OUKA

https://ir.library.osaka-u.ac.jp/

The University of Osaka

OSAKA UNIVERSITY

Interaction between Carbon and Extended Defects in Fe Studied by First-Principles Based Interatomic Potential

2021/06

Division of Precision Science & Technology and Applied Physics

Graduate School of Engineering

OSAKA UNIVERSITY

Pham Thi Dung

Interaction between Carbon and Extended Defects in Fe Studied by First-Principles Based Interatomic Potential

Supervisor: Assoc. Prof. Kazunori Sato

June, 2021

Acknowledgments

I am truly honored to submit my doctoral thesis for the degree of doctor at the Quantum Engineering Design Couse, Department of Precision Science and Technology, Graduate School of Engineering, Osaka University. This work has been carried out under the supervision of *Assoc. Prof. Kazunori Sato* at the Computational Material Design Area research group, Division of Materials and Manufacturing Science, Graduate School of Engineering, Osaka University. I would like to express my sincere thanks to *Assoc. Prof. Kazunori Sato* for accepting me as his student as well as for the support, guidance, and encouragement to complete this research. I also would like to thank *Dr. Nguyen Tien Quang* for giving helpful instruction, guidance, advice and inspiration during my PhD course.

I am very grateful to *Prof. Masaaki Sugiyama* and *Assoc. Prof. Tomoyuki Terai* at the Computational Material Design Area research group, Division of Materials and Manufacturing Science, Graduate School of Engineering, Osaka University for their valuable suggestion, discussion and reviewing my manuscript through this work.

I am thankful *Prof. Yoji Shibutani* at the Division of Mechanical Engineering, Graduate School of Engineering, Osaka University for his support, helpful discussion and encouragement in my PhD course.

I would also like to thank all past and present members of the Computational Material Design Area research group, Division of Materials and Manufacturing Science, Graduate School of Engineering, Osaka University, especially *Dr. Katsuhiro Suzuki*, *Dr. Ryo Yamada* for their suggestion, encouragement and helps.

Finally, I wish to express the deep appreciation to my family for their encouragements and understanding.

Osaka, June 10th, 2021

Student

Pham Thi Dung

TABLE OF CONTENTS

Acknowledgments ii

TABLE OF CONTENTS.....iii

LIST OF FIGURES v

LIST OF TABLES viii

LIST OF ABBREVIATIONS ix

Abstract xi

CHAPTER 1. INTRODUCTION..... 1

1.1. Overview of iron-based alloy 1

1.2. Lattice defects in steel 5

1.2.1. Point defect 5

1.2.2. Grain boundary 6

1.2.3. Dislocation 9

1.3. Purpose of thesis 12

CHAPTER 2. CALCULATION METHODS……..14

2.1. Density functional theory 14

2.1.1. Hohenberg - Kohn theorems.....16

2.1.2. Exchange-Correlation functionals 18

2.1.3. Solving Kohn-Sham equation.....19

2.2. Molecular dynamics 20

2.4. Method of analysis 26

2.4.1. Segregation energy 26

2.4.2. Voronoi volume and coordination number 27

CHAPTER 3. RESULTS AND DISCUSSION 29

3.1. Point defect 29

3.2. Grain boundary (GB) 32

3.2.1. Model of grain boundary 32

3.2.2. Grain boundary energy 34

3.2.3. Segregation sites 41

3.2.4. Segregation energy 42

3.3. Dislocation 45

3.3.1 Dislocation energy 47

3.3.3. Carbon segregation in dislocation 50

3.3.4 Local atomic structure and Carbon segregation 58

3.3.5 Compasion with other defects 60

CHAPTER 4. CONCLUSION 62

REFERENCES 64

PUBLICATIONS 70

LIST OF FIGURES

Fig. 1-1. Relation between elongation (ductility) and tensile strength in low carbon steels for general applications.[3] 3

Fig. 1-2. Two typical interstitial sites for C occupation in BCC Fe..... 5

Fig. 1-3. Description of grain boundary [19]. ***o*** *corresponds to the rotation axis,* ***ω*** *is misorientation angle,* ***n*** *is normal of grain boundary*..... 6

Fig. 1-4. a) Low angle grain boundary and b) High angle grain boundary in a cubic crystal [20]**.** 7

Fig. 1-5. The relationship between grain boundary energy (in mJ· $m-2$*) and misorientation angle (˚) in <110>STGB of BCC Fe and BCC W* [21]**.** 8

Fig. 1-6. Schematic model of a dislocation in supercell. 10

Fig. 1-7. Schematic model of an edge dislocation (side view) 11

Fig. 2-1. An illustration of the self-consistent field (SCF) 19

Fig. 3-1. C located at O-site in 1,2 positions and T-site in 3 position in Fe-V system..... 29

Fig. 3-2. Positions of carbon at O-site around iron vacancy. Orange balls present Fe atoms..... 30

Fig. 3-3. Grain boundary structures of a) modified Σ9(221)38.9˚ STGB and b) its optimized structure. The grain boundary is perpendicular to c-axis. Orange and gray spheres represent Fe atoms lying on two adjacent atomic layers along rotation axis (b - axis) 33

Fig. 3-4. Grain boundary energy as a function of misorientation angle. The GBE values calculated by Johnson potential are taken from previous study (ref[30])*.....35

Fig. 3-5. The grain boundary energy as a function of free volume......36

Fig. 3-6. Grain boundary energy of STGBs with C calculated by using classical interatomic potential 37

Fig. 3-7. Scanning planes (colored in pink on the left-hand side sub-figures) and dissolution energy landscapes (right-hand side sub-figures) of FeC systems of a) Σ3(112) STGB and b) Σ9(221) STGB. The location of GB is indicated by green dashed line......42

Fig. 3-8. The relationship between segregation energy and Voronoi volume of C in different STGBs. In this plot not only the C on the GB plane but also the C off the GB plane are included......43

Fig. 3-9. The segregation energy of C (left) and Voronoi volume (right) as functions of the distance between GB and C. The horizontal dashed line at the bottom of the right-hand side sub-figure indicates the Voronoi volume of C located at O-site in BCC bulk iron......44

Fig. 3-10. Quadrupole dislocation model. D corresponds to the distance of two adjacent dislocation cores.....46

Fig. 3-11. Dislocation energy as a function of distance D between two adjacent dislocation cores (proportional to the supercell size) of different dislocation configurations calculated by classical force-field method using the new Fe-C potential. 49

Fig. 3-12. Atomic model of the <100>(010) edge dislocation core and different interstitial sites. Black and white balls represent Fe atoms in two adjacent planes (plane A and plane B, respectively) along <001> direction. Solid

circles and dashed circles represent positions of C atom in plane A and plane B, respectively……50

Fig. 3-13. a) BCC Fe and basic unit cell of Fe with the corresponding O-sites where C resides and b) The colour map of the Voronoi volume of Fe around the dislocation core and the positioning levels of C under consideration at different layers referring from the glide plane......54

Fig. 3-14. Segregation energy of C in system containing ½<111>(110) edge dislocation with C at O-sites lying along a) TDA(001) and b) TDA(010) and TDA(100)......55

Fig. 3-15. Segregation of C in ½<111>(112) edge dislocation with one C in a) TDA(001) and b) TDA(010) TDA(100).Segregation energy of C in system containing ½<111>(112) edge dislocation with C at O-sites lying along a) TDA(001) and b) TDA(010) and TDA(100)......56

Fig. 3-16. Segregation of C in a) <100>{010} and b) <100>{011} edge dislocations at different layers from the glide plane......58

*Fig. 3-17 .Energy diagram of C in BCC Fe containing different defects....*61

LIST OF TABLES

Table 1: Different phases of steels based on carbon content.[5, 6] 3

Table 2. Optimal iron-carbon potential parameters. The parameters for pure iron and pure carbon interactions are taken from previous works[50] 26

Table 3. The segregation energy of C in O-site and T-site. $d_{\text{C-V}}$: Carbon vacancy distance Voronoi volume of C in O-site in perfect α-Fe: 7.05 Å^3 31

Table 4. Unit cell used for the DFT calculations on grain boundary energies of typical STGBs. Here, ω is misorientation angle, m is number of Fe in the unit cell. γGB^* values are obtained from previous DFT studies. 39

Table 5. Supercells used for the calculations using Tersoff/ZBL potential on various <110>STGBs.. The supercell size is indicated by using vectors $\boldsymbol{a0}$ and $\boldsymbol{b0}$ defined in Table 3. Grain boundary energy, segregation energy of C and Voronoi volume of C are also summarized. 40

Table 6. Structure of edge dislocations considered in the present study. L_x, L_y, L_z are basic unit cell size which create dislocation models, and b is the magnitude of Burgers vector. For each dislocation configuration, glide plane is perpendicular to slip direction. 47

Table 7. Dissolution energy of C in different types of defect structures..... 52

Table 8. Size of simulated supercell containing quadruple edge dislocations, segregation energy (Eseg) of C, Voronoi volume (V) around C and shortest Fe-C bond distance (dFe_C). m is number of Fe atoms in a simulation cell. Here, the supercell size is indicated by using size of basic unit cell of Lx, Ly, Lz..... 58

LIST OF ABBREVIATIONS

ABOP	Analytic bond-order potential
APT	Atom probe tomography
BCC	Body-centered cubic
BCT	Body-centered tetragonal
DFT	Density functional theory
DOF	Degrees of freedom
FCC	Face-centered cubic
GB	Grain boundary
GGA	General Gradient Approximation
HAGB	High angle grain boundary
LAGB	Low angle grain boundary
LAMMPS	Large-scale Atomic/Molecular Massively Parallel Simulation
LDA	Local density approximation
MS	Molecular statics
MD	Molecular dynamics
O-site	Octahedral site
STGB	Symmetrical tilt grain boundary
T-site	Tetragonal site

TDA	Tetragonal distortion axes
TEM	Transmission electron microscopy
VASP	Vienna Ab initio Simulation Package
ZBL	Ziegler-Biersack-Littmark

Abstract

Many mechanical properties of material are strongly depended on defects in structure of the material such as vacancies, dislocations and grain boudaries, which present space to accommodate impurity elements. For iron/steel materials, the location of foreign atoms in defect structure strongly affects to their strength and ductility. Therefore, the knowledge of location of C in iron/steel under the existence of defects is essential for material design.

In this study, the segregation of carbon is explored in α-Fe<110> symmetric tilt grain boundaries (STGBs) and several edge dislocations. Because of the limitation of number of atoms in density functional theory (DFT) calculation, in this work, the classical force-field method in conjunction with the presently constructed Tersoff/ZBL interatomic potentials have been used for performing the simulations of very large cells of STGBs and edge dislocations. Fe-C interatomic potential in the framework of Tersoff/ZBL potential has been constructed by fitting its parameters to reproduce the results of first-principles calculations of various BCC Fe systems with C and Fe vacancies.

Firstly, I have applied classical force-field simulations using the newly developed Tersoff/ZBL potential for calculating grain boundary energies. It is found that the present potential give the most adequate results in comparison with the DFT compared to the other standard classical potentials. The segregation sites of C are determined by examining the energy landscape of the GB systems, and it is found that C mainly locates at the GB planes. It is also found that more unstable grain boundary exhibits a stronger interaction with C. By using the Voronoi construction, it is suggested that there is a close correlation between the segregation energies of C and open space around C.

Next, in order to confirm the universality of the relation between open space around C and its segregation energy, I have calculated several edge dislocations and their interaction with C. It is found that the stabililty of different seven edge

dislocations with <111>, <100>, and <110> Burgers vector are reasonably reproduced experimental observations and the prediction by elastic theory. By calculating the segragtaion energy of C as a function of distance from dislocation core of calculated dislocations, it is shown that C is strongly trapped at dislocation core and dislocation exhibits as a long-range interaction with C comparing to STGBs. It is also found that the interaction between dislocations and C shows similar tendency to the case of STGBs, namely the stability of C around the dislocation is related to the Voronoi volume around C.

I summary calculated segregation energy of C in different defects by using the Tersoff/ZBL potential. I have also calculated the interaction between C and single Fe vacancy. In general, STGBs and edge dislocations trap C strongly compared to single Fe vacancy, and more unstable defect structures attract C more strongly. Among the presently calculated extended defects, the <100> edge dislocation is the strongest trap of C. The obtained tendency might offer useful guideline to analyse atomistic distribution of C in Fe with extended defects.

CHAPTER 1. INTRODUCTION

Today, thanks to the improvement in computational technology, researchers are making vigorous progress in the understanding of materials at atomic and molecular levels[1]. With this understanding, we can select suitable materials for specific purposes and also improve or even predict advanced materials for applications. Aiming at enhancing the collaboration between experimental research and simulation work in studying on existing and new materials as well as their application, computational material science with its techniques is applied to solve material relating problems. Moreover, in some aspects, computational experiments have an advantage over real experiments because most of the variables can be controlled in the calculations to simulate extreme conditions. Particularly, by analyzing the simulation results we can discuss underlining mechanism behind the functional properties. The calculation related to iron-carbon alloys is a good example to show the possibility of computational methods and contributes to the development of the fundamental research in steel industry, because the real lattice is not perfect and contains many types of defects such as vacancy, dislocation and grain boundary. Those defected systems show great importance to improving the properties of materials. Regarding the requirement of understanding the behaviour of impurity atoms and their influence to mechanical properties of iron, we have investigated the relation of carbon segregation and local structure of several defected structures of BCC Fe.

1.1. Overview of iron-based alloy

Iron-carbon alloy or steel is one of the most widely used structural materials in our society. The versatility, durability and strength of steel can meet requirements for a variety of purposes, and it is also an affordable price and

environmentally friendly[2]. The steel industry has a long history and an extraordinary development, which can be classified into three generations. Those three steel grades are classified according to their important properties, namely strength (load capacity) and ductility (an index for plastic formability)[3]. The first generation consists of the conventional steels such as IF (Interstitial Free), HSLA (High-Strength Low-Alloy) steels and the advanced high strength steels (AHSS) such as DP (Dual Phase), TRIP/TWIP (Transformation or Twinning Induced Plasticity) steels. As shown in Fig. 1-1, the conventional steels are characterized by high ductility but low strength while the advanced high strength steels have high strength but less ductility. The second generation is so-called the austenitic-based steels which are known for their high strength and good tensile properties. The austenitic-based steels are developed by alloying expensive elements such as Ti or Al, leading to the high cost of manufacturing and production. Nowadays, new steels combining both high strength and high ductility with low cost are still under investigation and development. Improving their mechanical properties by modifying polycrystal structures of Fe matrix or controlling doped impurity atoms is an attractive and active research field.[2, 3]

Among impurities used in the production processes of iron/steels, carbon is one of the most important foreign interstitial atoms determining the strength and hardness of steels even though its concentration is quite low as 0.022 wt% in body-centered cubic (BCC)- Fe [4]. The concentration of C and its diffusion in Fe matrix control the formation and kinetics of many important phases and phase transformations in steel. The influence of C on different phases of steels is summarized in Table 1.

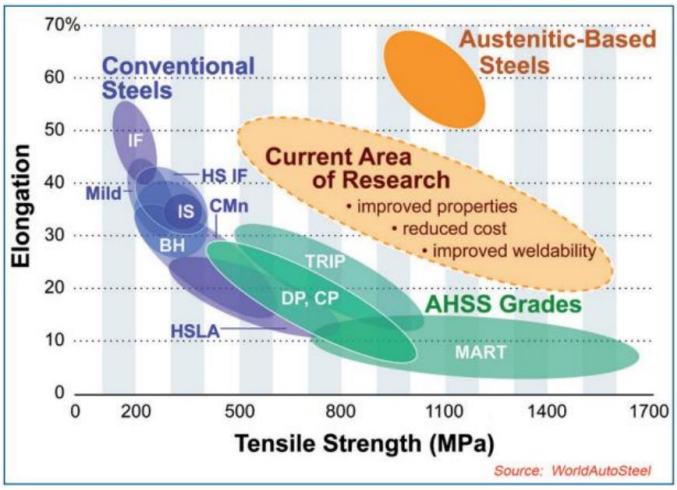

Fig. 1-1. Relation between elongation (ductility) and tensile strength in low carbon steels for general applications.[3]

Table 1: Different phases of steels based on carbon content.[5, 6]

Phase	Term	Structure	Temperature conditions	Notes
α-Fe	Ferrite	BCC	$T < 922.50$ ˚C	Solubility is very low
γ-Fe	γ-Ferrite	FCC	911.50 ˚C < T < 13960 ˚C	C is an "Austenite stabilizer": add C, γ field widens
δ-Fe	δ-Ferrite	BCC	13920˚C<T<15360 ˚C	Dissolve as much as 0.08% of carbon
Fe_3C	Cementite	Orthorhombic		Hard ceramic
Fe-C solute solution	Martensite	BCT		Metastable, formed by quenching

The concentration of C determines the strength and ductility of steels[7]. Alloys containing more than 2.0wt% of C content are considered as cast irons, which are known as very hard materials and they are also very brittle. In the case of carbon concentration of less than 0.08wt%, the steel becomes softer when compared to cast iron, but its ability of incurvation or distortion is better without breaking, which is necessary for steel to play a role as a structural material in the construction of buildings and other infrastructures. When carbon concentration is between 0.2wt% and 2.0wt%, the properties of steel become special owing to the balance between hardness and ductility. The appearance of carbon atoms in the iron system even in small quantities is still considered to have a significant effect on the energetics and kinetic properties of the system. The formation of carbides occurs by exceeding the limit of carbon solubility, which contributes significantly to the improvement of the durability and hardness of steel. Beside, when the carbon concentration in the system is below the solubility limit, the thermal and mechanical properties of the system can be changed significantly only by a minimal amount of carbon atoms (several tens of ppm) at interstitial sites [8].

At room temperature, α-Fe (ferrite) exists as the body-centered cubic structure containing two atoms per conventional cubic unit cell where one Fe is located at coordinates ($a_{Fe}/2$, $a_{Fe}/2$, $a_{Fe}/2$) (a_{Fe} is lattice constant of α-Fe) and the other is placed at the origin of the cell with coordinates (0, 0, 0) (Fig. 1-2). As for C in α-Fe, typical locations are octahedral (O-site, the most stable site) and tetrahedral (T-site, a metastable site) sites (Fig. 2). It is known that the formation energy of octahedral C interstitial is very high therefore many experimental and theoretical studies have been devoted to identifying the location of C in Fe. It is particularly interesting to study the interaction between C and various kinds of defects in Fe and elucidate whether these defects affect the location of C [9,10]. This is because in the fabrication process of steel-related materials various types of

defects, such as vacancies, dislocations or grain boundaries, are naturally expected to exist. Those defects are studied as attractive sources for C in α-Fe.

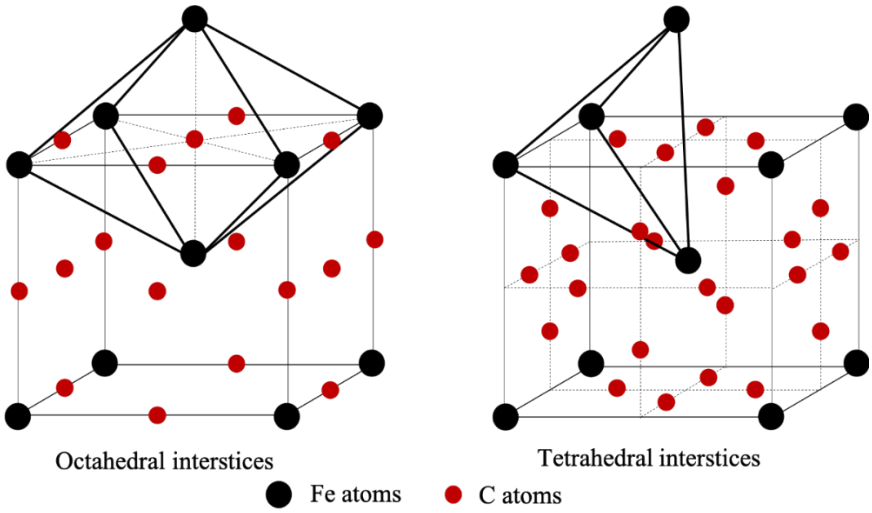

Fig. 1-2. Two typical interstitial sites for C occupation in BCC Fe.

1.2. Lattice defects in steel

1.2.1. Point defect

Point defect (zero-dimensional defect) is a type of lattice defects that occurs at a single lattice point. In BCC metal alloys such as W and Fe alloys, the strong interaction of C with vacancy (V) has been investigated with great scientific and technological interests to understand the nucleation, evolution, and kinetics of the other defects [11,12,13]. In the previous simulations, it was found that C at O-site interacts strongly with vacancies whereas its interaction with self-interstitial atoms (C at vacancy) has been explored to be weaker but also attractive comparing to the perfect case [12]. Significant reduction of vacancy diffusion due to the presentation of C has been insighted. The binding energy of C-V and the migration of vacancy in α-Fe have been estimated by *ab initio* calculations[14,12] as well as classical force-field method by using various Fe-C interatomic potential

models [15,16,17]. The C-V binding energy values of 0.41~1.1eV and vacancy migration energies of 0.55~1.28 eV in Fe have been explored [18,10]. In this work, the interaction of C and vacancy is investigated by a newly constructed FeC interatomic potential.

1.2.2. Grain boundary

A grain boundary (GB) is an interface which separates two grains with the same crystal structure but different orientations. It can be fully described by five macroscopic and three microscopic degrees of freedom (DOFs). The five macroscopic DOFs specify the crystallography of the GB, with three of them representing the misorientation relationship between the two grains (two for the rotation axis ***o*** and one for the rotation angle ***ω***) and the remaining two defining the orientation of the GB plane ***n***.

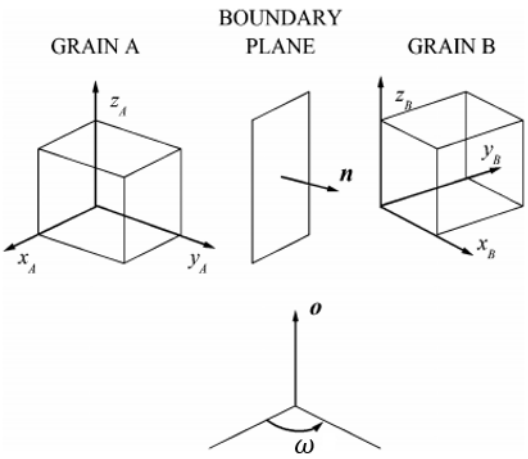

*Fig. 1-3. Description of grain boundary [19]. **o** corresponds to the rotation axis, **ω** is misorientation angle, **n** is normal of grain boundary.*

A GB is referred to as a tilt/twist GB when the rotation axis is parallel/perpendicular to the GB plane. If the Miller indices of a tilt GB plane are identical for the two grains, namely, $\{h_1k_1l_1\}=\{h_2k_2l_2\}$, the GB is called a symmetrical tilt grain boundary (STGB) in contrast to asymmetrical tilt GB.

According to the misorientation angle, the GBs can be classified into low and high angle GBs. The low angle grain boundary (LAGB) exhibits as an edge dislocation (Fig 1-4a). The angle $\boldsymbol{\omega}$ is related to the spacing between dislocations as the following equation:

$$\boldsymbol{\lambda_d} = \frac{\boldsymbol{b}}{\mathbf{2}\,\mathbf{sin}\left(\frac{\boldsymbol{\omega}}{\mathbf{2}}\right)} \cong \frac{|\boldsymbol{b}|}{\boldsymbol{\omega}} \tag{1.1}$$

where $\boldsymbol{b}$ is magnitude of Burger's vector of the dislocation. When the misorientation angle is larger than 15°, the high angle grain boundary (HAGB) is established (Fig. 1-4b), and the dislocation model of a grain boundary become incorrect. We can completely describe a grain boundary by the notation $\boldsymbol{\omega}°[\boldsymbol{h_o k_o l_o}], (\boldsymbol{h_{nA} k_{nA} l_{nA}})$ in which, the rotation axis is $\boldsymbol{o}$ = $[\boldsymbol{h_o k_o l_o}]$ and $(\boldsymbol{h_{nA} k_{nA} l_{nA}})$ is Miller index of grain A.

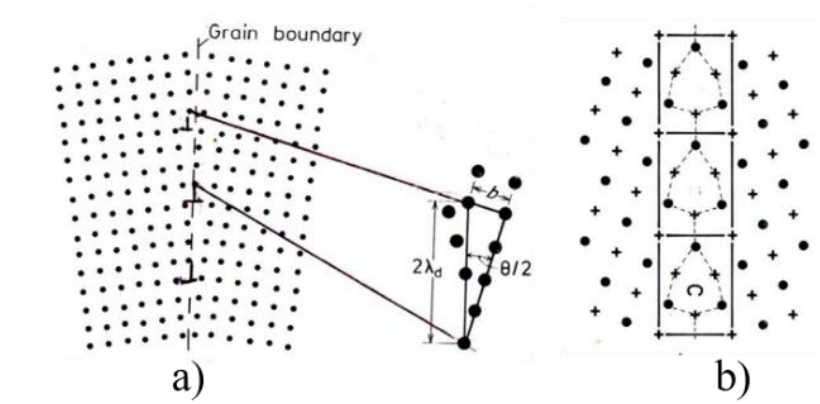

Fig. 1-4. a) Low angle grain boundary and b) High angle grain boundary in a cubic crystal [20]**.**

In grain boundary model, for a certain misorientation angle, some lattice points of grain A coincide exactly with some lattice points of grain B, this is indicated as **coincidence site lattice** (CSL) Σ value. With Σ equals to 1, no grain

boundary occurs, it means a perfect crystal structure. The Σ3 value is considered as a twin grain boundary which is known as the most stable GB with smallest grain boundary energy. The dependence of misorientation angle $\boldsymbol{\omega}$ and grain boundary was investigated and shown in Fig. 1-5 [21] which indicated that the smallest GB energy is obtained for Σ3(112).

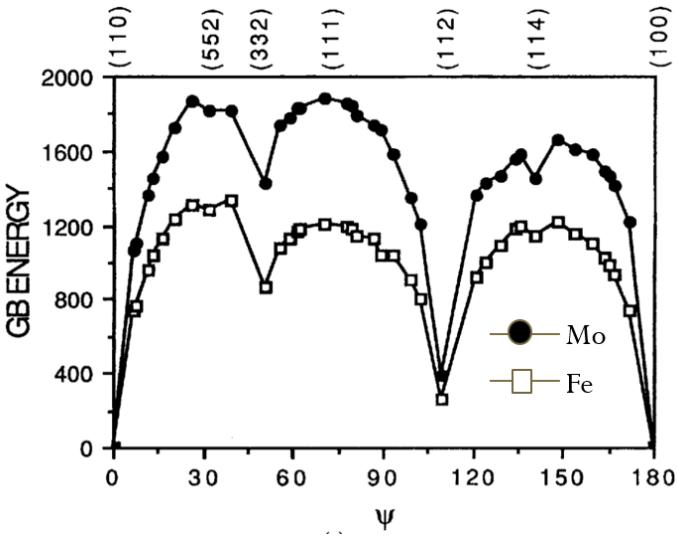

Fig. 1-5. The relationship between grain boundary energy (in mJ·m^{-2}) and misorientation angle (°) in <110>STGB of BCC Fe and BCC W [21].

Experimentally, C is well known to enhance the stability of GBs in steels, in contrast to H, P and S, thereby improving its crack-resistant properties [22, 23, 24]. Hence, to control the strength of steel, it is important to investigate the interaction between GBs and C [25]. In addition, the segregation of carbon causes the formation of carbon clusters and the precipitation of carbides in aging process, and it affects the mechanical properties of carbon steel [26]. However, the experimental assignment of the location of carbon is still difficult. So far, the GBs have been visualized by using transmission electron microscopy (TEM) and atom probe tomography (APT) [27, 28]. The excess of carbon at the GBs was detected by combining the mass spectroscopy and ion projection microscopy in

grain boundary space and the linear relationship was observed between solubility of C and misorientation angle $\boldsymbol{\omega}$ for $\boldsymbol{\omega} < 25^{\circ}$ in α-Fe GBs [29]. However, such kind of correlation has not been found for large $\boldsymbol{\omega}$-GBs. Since the local atomic structure depends strongly on $\boldsymbol{\omega}$, it is desirable to investigate the correlation between local atomic structure of GBs and the stability of carbon at the GBs. For this purpose, numerical simulations might be helpful to complement the experimental observations. As for the computational approaches, the stability of various pure α-Fe <110> symmetric tilt grain boundaries (STGBs) with common <110> tilt axis was investigated by performing the molecular dynamics simulations with several classical interatomic potentials of Fe such as the pair potential proposed by Johnson [21, 30] or Embedded Atom Method (EAM) [31] potential, however the behaviour of impurity atoms has been studied only in a few typical α-Fe <110> STGB configurations [32, 33, 34] due to the lack of universal and reliable interatomic potentials for the systems with impurities. Grain boundary (two-dimensional defect or plane defect) significantly affects the physical and mechanical properties of polycrystalline materials[35, 36].

1.2.3. Dislocation

Dislocation is a line defect whose structure can be characterized by a line (Fig. 1-6).

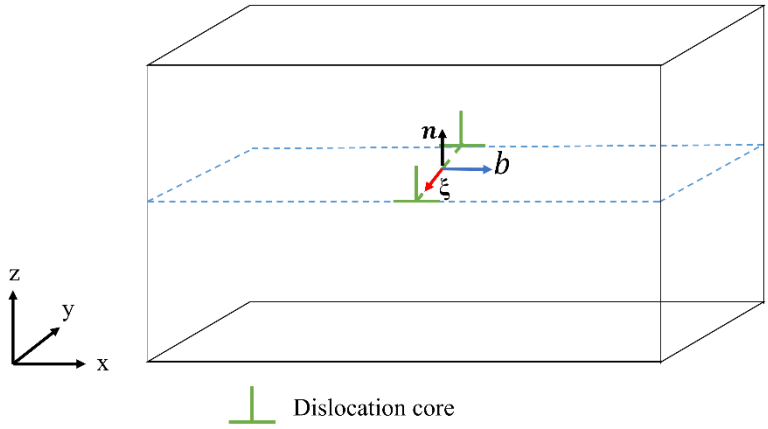

Fig. 1-6. Schematic model of a dislocation in supercell.

A dislocation can be identified by knowing Burgers vector ***b*** and glide plane (xy plane in case of Fig.1-6). In Fig. 1-6, ξ is direction of dislocation line, ***n*** is a normal vector to the glide plane. Basically, there are two types of dislocations: edge and screw dislocations. The edge dislocation is disruption in the crystal structure by an extra half plane of atoms inserted between the regular atom sequence, resulting in a dislocation line. For the edge dislocation, the Burgers vector ***b*** is normal to the dislocation line ξ. This extra array of atoms leads to a distortion and affects the local structure so that compressed part and expanded part always appear along *z* direction as shown in Fig. 1-7. The screw dislocation can be formed by rotating a half of the upper part of the crystal to right related to the lower part. For the screw dislocation, the Burgers vector ***b*** is aligned with the dislocation line ξ. In this thesis we focus on the edge dislocations. A dislocation can be denoted by $<h_o k_o l_o>(h_n k_n l_n)$ in which $h_o k_o l_o$ is Burgers vectore ***b*** and $h_n k_n l_n$ is Miler index of glide plane.

An edge dislocation can be constructed by superimposing two crystals with different number of atomic layers. The top part contains an extra atomic layer compared to the bottom one. Therefore, in order to maintain the same length along X (Burgers vector) of both upper and lower parts, the structure of the top

part is always compressed while that of the lower part is always expanded as compared to pure bulk structure (Fig.1-7).

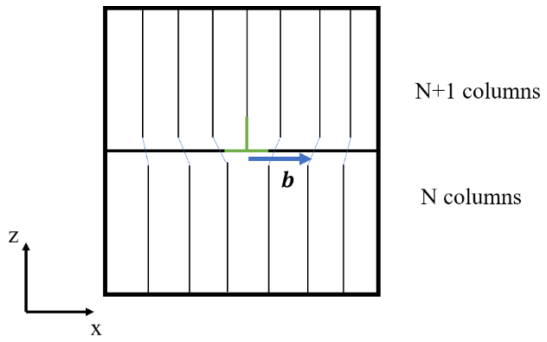

Fig. 1-7. Schematic model of an edge dislocation (side view)

Dislocation (one-dimensional defect or line defect) can be observed by using X-ray diffraction[37], transmission electron microscopy (TEM) [38] or scanning transmission electron microscope (STEM)[39].

It is well known that the creation and motion of dislocations are the fundamental mechanism of plastic deformation. The influence of impurity atoms and vacancies to the mobility of dislocation core leads to significant change in mechanical properties of materials. In BCC metal, the dislocations with Burger vector <111> are usually observed in experiments [40]. Therefore, many previous studies focused on ½<111> dislocation by using classical interatomic potentials [41]. In steel, the interaction of dislocation with C impurity has attracted a large attention from scientific community. The most popular edge dislocation model ½<111>$(1\bar{1}0)$ which is also known as the most stable dislocation in BCC Fe has been studied with C segregation. The C and dislocation interaction was simulated in the ½<111>$(1\bar{1}0)$ dislocation using the pairwise interatomic potentials for Fe-C pair proposed by Johnson[23]. The results showed that C atoms interact with dislocation between the {110} atomic planes with interaction ennergy of -0.7 eV. In addition, based on density-functional theory (DFT), the formation of strong

covalent-like bonds between C and adjacent Fe was investigated for ½<111> and <100> edge dislocations, thereby leading to formation of carbon–dislocation complexes [42]. However, the atomistic mechanism of stability of dislocation configuration, for example the relation of C location and local atomic structure of dislocation, has not been clearly understood yet.

1.3. Purpose of thesis

In this thesis, I try to predict the location of C in BCC Fe with some typical types of defects, namely vacancy, α-Fe <110> STGB, and edge dislocation structures of α-Fe, and clarify the relation between the stability of C and its local structures. First-principles calculations based on the density-functional theory have been widely applied to give highly accurate prediction and insight into atomic behaviour of impurity segregation. However, it is computationally too expensive to apply the DFT to complex STGB and dislocation systems. Therefore, alternative methods in conjunction with classical force-field have been employed, namely classical interatomic potential for Fe-C systems was constructed within the framework of Tersoff/ZBL potential by fitting its parameters to reproduce the results of first-principles calculations of various α-Fe systems with C and Fe vacancies.[24,25)] The reliability of the new Tersoff/ZBL potential is demonstrated by comparing the grain boundary energy and binding energy of V-C pair with those obtained by DFT. The results are also compared with those calculated by other interatomic potentials. In the analysis of the segregation sites of carbon in α-Fe, the relation between local atomic structure and stability of C is discussed by considering the free volume around C based on the Voronoi construction, the shortest bond length from C to its neighbors Fe and the coordination number. By using the same interatomic potential, the interaction of C with different defects has been systematically investigated to identify the priority position of C in mutiple defects systems.

This thesis is organized as folows. In Chapter 2, we introduce the computational methods applied in this thesis. The results and discussion are given in Chapter 3. Here, the stable position of C in vacancy system is firstly studied. After that, the stability of GBs with and without C and the segregation of C in GBs systems are estimated. The dislocation model, stability of different dislocation configurations and C segregation at dislocation core are discussed in the third part of Chapter 3. At last, the conclusion and outlook are given in Chapter 4.

CHAPTER 2. CALCULATION METHODS

2.1. Density functional theory

Density functional theory is one of the most popular and successful quantum mechanical approaches to matter. Nowadays, it is regularly applied for calculating the binding energy of molecules in chemistry and the band structure of solid in physics. DFT is a method used to solve the Schrodinger's equation of N_e -electron systems (N_e can be up to thousands) with the support of High Performance Computer (HCP). The Schrodinger equation is the basic tool to study the properties of a given material. The time-independent Schrodinger equation has the operator form:

$$H\Psi = E\Psi \tag{2.1}$$

Where H is the Hamiltonian operator, E is energy, and Ψ is the wave function. This equation can be exactly solved in the case of one nucleus and one electron.

Let us consider a system including N nuclei of Z_n charge at position $\{R_n\}$ for $n = 1, \dots, N$ and M electrons at position $\{r_i\}$ for $i = 1, \dots, M$. The many-body wave function Ψ becomes:

$$\Psi = \Psi(R_1, R_2, R_3, \dots, r_1, r_2, r_3, \dots)$$

To calculate and simulate a quantum system, we have to solve the Schrodinger equation with $3N$ variables. In the system having many electrons, the solution of this equation becomes very complicated and could take a long calculation time, requiring High Perform Computer. The Hamiltonian for the whole bulk system is:

$$H = -\frac{\hbar^2}{2}\sum_k \frac{\nabla^2}{M_k} + \frac{1}{2}\sum_{k\neq l}\frac{Z_k Z_l}{|\boldsymbol{R}_k - \boldsymbol{R}_l|} - \frac{\hbar^2}{2m_e}\sum_i \nabla_i^2 + \frac{1}{2}\sum_{i\neq j}\frac{e^2}{|\boldsymbol{r}_i - \boldsymbol{r}_j|} - \sum_{i,k}\frac{Z_k}{|\boldsymbol{r}_i - \boldsymbol{R}_k|} \tag{2.2}$$

Where $\hbar = h/2\pi$, h is the Planck constant, m_e and $\boldsymbol{r}_k$ denote the electron mass and the respective coordinates, M_k and $\boldsymbol{R}_k$ are nuclear masses and the respective coordinates, and Z is the charge of the nuclei. The indices i and j indicate electrons ith and jth while k and l denote the kth and lth nuclei. The first term in Eq. 2.2 denotes the kinetic energy of the nuclei, the second term is the Coulomb energy between the nuclei, the third term labels the kinetic energy of the electrons, the fourth term indicates the Coulomb interaction among the electrons, and the last term denotes the electrostatic interaction between the electrons and the nuclei. So, in short, Eq (2.2) can be rewritten as:

$$H = T_n + V_{nn} + T + V_{int} + V_{ext} \tag{2.3}$$

Where T, T_n are the kinetic energies of the electrons and nuclei, respectively. The potential energies from electron-electron repulsions, nuclear-nuclear repulsion, and electron-nuclear attraction are labelled as V_{int}, V_{nn}, and V_{ext} , respectively. Therefore, from above equations, the calculation of Hamiltonian for many-body system is a complex process. In practice, a series of approximation methods is made to reduce the complexity of the calculation. The first approximation is Born-Oppenheimer approximation where the nuclei are considered to be stationary, and Eq. 2.2 has to be solved for the electrons around these stationary nuclei. This allows us to remove the first term in Eq. 2.2. The second term is only a constant (since the nuclear positions are known). Following the Born-Oppenheimer approximation, Eq. 2.2 and 2.3 can be expressed:

$$H_{elec} = T + V_{int} + V_{ext} \tag{2.4}$$

$$H_{elec} = -\frac{h^2}{2m_e}\sum_i \nabla_i^2 + \frac{1}{2}\sum_{i\neq j}\frac{e^2}{|\boldsymbol{r}_i - \boldsymbol{r}_j|} - \sum_{i,I}\frac{Z_I.e}{|\boldsymbol{r}_i - \boldsymbol{R}_I|} \tag{2.5}$$

$$H_{elec} = -\frac{h^2}{2m_e}\sum_i \nabla_i^2 + \frac{1}{2}\sum_{i\neq j}\frac{e^2}{|\boldsymbol{r}_i - \boldsymbol{r}_j|} - \sum_i V_{ext}(\boldsymbol{r}_i) \tag{2.6}$$

Through the Born-Oppenheimer approximation, the complex Hamiltonian H is simplified to the electron Hamiltonian H_{elec}. Now, many-body wave-

function is dependent on spin and positions of the electrons while component V_{ext} (external potential) depends on the positions of nuclei.

2.1.1. Hohenberg - Kohn theorems

Material properties are mostly exhibited through the ground-state electronic structure. The ground-state is governed by the electrons surrounding nuclei and the interactions between them. Hence, if we can get hold of the real space distribution of these electrons (the electron charge density $\rho\ (\boldsymbol{r})$) then almost all physical properties can be predicted. The objective of the electronic structure calculations is to obtain the electron density. This is the main idea of DFT. The total number of electrons, n_e is:

$$\int \rho\ (\boldsymbol{r}) d\boldsymbol{r} = n_e \tag{2.7}$$

The density functional theory is based on two theorems. The first one was introduced by Hohenberg and Kohn, and the second one was extended by Kohn and Sham.

Theorem 1

The external potential $V_{ext}(\boldsymbol{r})$ is univocally determined by the electronic density, besides a trivial additive constant:

$$E = E[\rho(\boldsymbol{r})] = \int V_{ext}\ (\boldsymbol{r})\rho(\boldsymbol{r})d\boldsymbol{r} + F[\rho(\boldsymbol{r})] \tag{2.8}$$

$F[\rho(\boldsymbol{r})]$: functional of the charge density,

where the external potential (V_{ext}) presents the interaction of the electrons and the nuclei. Furthermore, the $\rho(\boldsymbol{r})$, $F[\rho(\boldsymbol{r})]$ terms are the kinetic energy of the electrons and the inter-electron interactions, respectively, indicated three-

dimensional electron density. However, unless we know $F[\rho(\boldsymbol{r})]$ term, we still do not have all the necessary information to calculate the ground-state energy of a many-electron system.

Theorem 2

The functional $E[\rho(\boldsymbol{r})]$ has its minimum value (the ground-state) for the actual electron-change density of the system.

The Hohenberg-Kohn theorems laid the foundation of DFT. In 1956, Kohn and Sham introduced a method in order to solve the Schrodinger equation via a series of equations, known as Kohn-Sham equation, it is:

$$F[\rho(r)] = E_{ke}[\rho(r)] + E_H[\rho(r)] + E_{xc}[\rho(r)] \tag{2.9}$$

where E_{ke} denotes the kinetic energy of electron, E_H represents the Coulombic energy of electron-electron interaction. E_{xc} is the exchange-correlation term, represents all unknown terms. By defining electron density term, the one electron Schrodinger-like equation is rewritten:

$$\left[-\frac{\hbar^2}{2m_e}\nabla^2 + V_{eff}(\boldsymbol{r})\right]\varphi_i(\boldsymbol{r}) = \epsilon_i\varphi_i \tag{2.10}$$

where ϵ_i denotes the orbital energy, φ_i represents the Kohn-Sham orbital, and the effective potential is symbolized as V_{eff}. The effective potential is expressed as:

$$V_{eff}(\boldsymbol{r}) = V_{ext}(\boldsymbol{r}) + \int \frac{\rho(\boldsymbol{r}')}{|\boldsymbol{r}-\boldsymbol{r}'|} d\boldsymbol{r}' + V_{xc}(\boldsymbol{r}) \tag{2.11}$$

where the $V_{xc}(\boldsymbol{r})$ represents the exchange-correlation potential, which can be related to the exchange-correlation energy functional ($E_{xc}[\rho(\boldsymbol{r})]$) by the following equation:

$$V_{xc}(\boldsymbol{r}) = \left(\frac{\delta E_{xc}[\rho(\boldsymbol{r})]}{\delta(\rho(\boldsymbol{r}))}\right) \tag{2.12}$$

For an arbitrary electron charge density, there is no simple explicit expression for the exchange-correlation energy E_{xc}. The local density approximation (LDA) and the generalized gradient approximation (GGA) are simple approaches to the exchange-correlation energy E_{xc}.

2.1.2. Exchange-Correlation functionals

In the Kohn-Sham equation, the exchange-correlation energy E_{xc} is an indeterminate component, thus an approximation is required. Various approximation methods have been used in order to approach this problem. The local density approximation, the generalised gradient approximation or the hybrid functional (for instance HSE - Heyd–Scuseria–Ernzerhof) approximations are recently used for estimation of $E_{xc}[\rho(\boldsymbol{r})]$ term.

The LDA exchange-correlation functional is expressed as:

$$E_{xc}^{LDA}[\rho] = \int \rho(\boldsymbol{r})\varepsilon_{xc}^{hom}\left(\rho(\boldsymbol{r})\right)d\boldsymbol{r} \tag{2.13}$$

The assumption of the LDA is that the exchange-correlation energy per electron, located at point $\boldsymbol{r}$, is equivalent to the homogeneous electron gas with density $\rho(\boldsymbol{r})$. Although simple, the LDA's results are good at description of bond length, crystal structure, elastic properties for various systems. However, the LDA is not accurate enough for simulating chemical energies (often overestimates binding energy).

The GGA exchange-correlation functional is expressed as:

$$E_{xc}^{GGA}[\rho] = \int \rho(\boldsymbol{r})\varepsilon_{xc}^{GGA}\left(\rho(\boldsymbol{r})\right), \nabla\rho(\boldsymbol{r}))d\boldsymbol{r} \tag{2.14}$$

The GGA's results are equivalent to LDA's in terms of atomic structure but the GGA has overcome the error of determining binding energy in LDA calculation. Moreover, the GGA describes band gaps of materials more

accurately compared to the LDA, but it generally underestimates the value of band gaps.

The hybrid functional is a combination of Hartree-Fock exchange energy and DFT exchange-correlation energy by the following equation:

$$E_{xc} = (1 - a)E_{xc}^{DFT} + aE_{x}^{HF} \tag{2.15}$$

The hybrid functional is claimed to be an effective way to describe band gaps of almost materials reasonably, especially semiconductors.

2.1.3. Solving Kohn-Sham equation

The exact ground-state density of the interacting system may be obtained by solving a non-interacting problem in which the potential V_{ext} depends on the electron density. Therefore, these simultaneous equations should be solved self-consistently. The calculation process follows the diagram below:

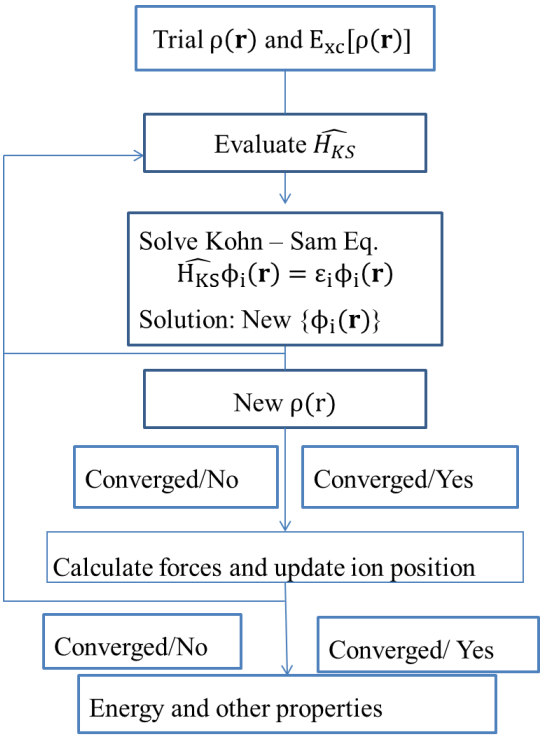

Fig. 2-1. An illustration of the self-consistent field (SCF)

2.2. Molecular dynamics

The molecular dynamics (MD) method was first introduced by Alder and Wainwright in the late 1950s to study the interactions of hard spheres [43,44]. Recently, due to the revolutionary advances in computer technology and algorithmic improvements, molecular dynamics has subsequently become one of the principal tools in many areas of physics, chemistry, biology and materials science. There are two main families of molecular dynamics methods, which are categorized based on model chosen to represent a physical system. One is classical molecular dynamics (CMD) and the other is quantum or *ab initio* molecular dynamics (QMD). In the classical molecular dynamics, atoms/molecules are treated as classical objects and ruled by the laws of classical mechanics. While in quantum molecular dynamics, which was introduced in the 1980s by Car and Parinello [45], the quantum mechanical effect of the electrons is included in the calculation of energy and forces for the classical motion of the nuclei. The quantum version gives an important improvement over the classical approach. However, it requires more computational resources and the size of simulated system is limited to few hundreds of atoms. For the simulation of systems comprising many thousands (or millions) of atoms, which are usually found in biology and materials science fields, the classical molecular dynamics approach is more practical.

Equations of motion

The classical molecular dynamics method (hereafter, shortly called molecular dynamics) is based on the Newton's second law. We begin with a system of particles which is governed by the Newton's equations of motion (EOM):

$$\boldsymbol{F}_i = m_i \boldsymbol{a}_i \tag{2.16}$$

where $\boldsymbol{F}_i$ is the force exerted on particle, m_i is the mass of particle and $\boldsymbol{a}_i = \frac{d^2\boldsymbol{r}_i}{dt^2}$ is the acceleration of particle i.

The computation of the force involves the calculation of the derivative (the gradient) of the interacting potential $U(\boldsymbol{r}_1, \boldsymbol{r}_2, \dots, \boldsymbol{r}_N)$, which is a function of the atomic positions $\boldsymbol{r}_i$ of all the atoms in the system, with respect to the atomic position:

$$\boldsymbol{F}_i = -\nabla_i U(\boldsymbol{r}_1, \boldsymbol{r}_2, \dots, \boldsymbol{r}_N) = -\frac{\partial U}{\partial \boldsymbol{r}_i} \tag{2.17}$$

Combining (2.16) and (2.17), we have

$$\frac{d^2 \boldsymbol{r}_i}{dt^2} = -\frac{1}{m_i}\frac{\partial U}{\partial \boldsymbol{r}_i} \tag{2.18}$$

The essential task in molecular dynamics simulation is to solve the above equations of motion (the second order differential equations). With a given interacting potential, one can find the trajectories of the particles for an interval time frame as well as the velocities of the particles and other physical quantities (both micro- and macroscopic).

2.3. Classical potentials

To understand the role of carbon in complex defect systems of α-Fe, it is important to consider atomistic modelling at large time and length scale. This can be done using molecular dynamics or Monte Carlo simulations in conjunction with empirical potentials. In the past, some Fe-C empirical potentials have been derived with requirements to find the total energy and the equilibrium state of the system. Johnson et al.[8] derived two-body central potentials for the FeC systems. The metal-metal and the metal-carbon interactions were described by pairwise potentials while no carbon-carbon interaction was assumed. Recently, one has used a more realistic potential for Fe, constructed based on the tight binding second moment approximation, achieving a better calculation of elastic properties and a more natural agreement with experimental data. Below, some advanced models for empirical potentials are introduced.

2.3.1. EAM potential

The total energy formalism of a system described by the embedded atom method (EAM) potential is shown below [46]:

$$E_{tot} = \sum_i F_i(\emptyset_i) + \frac{1}{2}\sum_i \sum_{i \neq j} \varphi_{ij}(r_{ij}) \qquad (2.19)$$

Where F_i is called the embedding energy, which is the energy required to embedded atom i into the electron density $\emptyset_i$ caused by surrounding atoms. The embedding energy is effective to describe the metallic bonding. The term $\varphi_{ij}(r_{ij})$ is a simple pair potential which is typically attributed to attractive and repulsive interactions between two atoms i and j with distance r_{ij}.

In general, the EAM potential for Fe-C reproduces the equilibrium lattice constants, the bulk moduli and the cohesive energies for some carbides. But it is failed to predict the most stable position of C in α-Fe[47].

2.3.2. Tersoff/ZBL potential

The classical interatomic potential for Fe-C systems which is mostly used in this work is constructed within the framework of Tersoff/ZBL potential. The Tersoff potential is an analytic bond-order potential which was found as a suitable potential model for metallic/non-metallic compounds[48]. The Tersoff/ZBL interatomic potential of Fe-C was constructed by fitting its parameters to reproduce, as much as possible, the forces and energies of DFT calculations of C in bulk BCC Fe with and without Fe vacancy. This potential was shown to be effective in reproducing C diffusion paths in BCC Fe as well as the effect of C on the BCC/FCC phase transformation in iron [49, 50].

In the Tersoff/ZBL potential framework, total potential energy of a given system is calculated by:

$$E = \sum_i E_i = \frac{1}{2}\sum_{i \neq j} V_{ij} \tag{2.20}$$

$$V_{ij} = f_C(r_{ij})[a_{ij} f_R(r_{ij}) + \mathrm{b}_{ij}\ f_A(r_{ij})] \tag{2.21}$$

where the potential energy is decomposed into site energies E_i or bonding energies V_{ij}. The i and j are the indices of atoms in the system with a spacing distance r_{ij}. The functions f_A and f_R are the attractive and repulsive Morse-type pair potentials, respectively, and the extra term f_C is a smooth cut-off function to limit the interaction range of the potential within a finite distance [51].

$$f_R(r) = \frac{D_0}{S-1}\exp[-\beta\sqrt{2S}(r - r_0)] \tag{2.22}$$

$$f_A(r) = \frac{SD_0}{S-1}\exp[-\beta\sqrt{2/S}(r - r_0)] \tag{2.23}$$

$$f_C(r) = \begin{cases} 1, r \leq R - D \\ \frac{1}{2} - \frac{1}{2}\sin\left[\frac{\pi}{2}\frac{(r-R)}{D}\right], R - D < r \leq R + D \\ 0, r > R + D \end{cases} \tag{2.24}$$

Here, r_0 and D_0 are the bond distance and bond energy for the dimer, respectively. The parameter β can be calculated by oscillation frequency of the dimer at ground state, from the expression [52]:

$$\beta = k\frac{2\pi c}{\sqrt{2D_0/\mu}} \tag{2.25}$$

where k, μ are the wave number and the reduced mass, respectively. The adjustable parameter, S can be estimated by using Pauling criterion:

$$E_b = -D_0\exp[-\beta\sqrt{2S}(r_b - r_0)] \tag{2.26}$$

here r_b is the equilibrium bonding distance and E_b is the energy per individual bond.

The parameters R and D are chosen as to contain the first-neighbor shell only for considered structure (for carbon $R = 1.8$ Å). The f_c function declines from 1 to 0 in the range $R - D < r < R + D$.

The major characteristic of this potential is the appearance of the b_{ij} part which includes three-body interactions and angularity. This bond-order term is expressed as:[51]

$$b_{ij} = \left(1 + \xi_{ij}\right)^{-\frac{1}{2}} \tag{2.27}$$

where:

$$\zeta_{ij} = \sum_{k \neq i,j} f_C(r_{ik}) g_{ik}(\theta_{ijk}) \omega_{ijk} \exp[\alpha_{ijk}(r_{ij} - r_{ik})] \tag{2.28}$$

is defined so that the effect is zero to the first order between the different bond lengths. Here, parameters ω_{ijk} and α_{ijk} are set relying upon the types of atoms on triplet (i, j, k). For instance, they are fitted to 1 for ω_{ijk} and 0 for α_{ijk} in the iron-carbon system.

The angular function $\mathrm{g}(\theta)$ is obtained by:

$$g(\theta) = \gamma \left[1 + \frac{c^2}{d^2} - \frac{c^2}{d^2 + (h - \cos\theta)^2} \right] \tag{2.29}$$

Here, θ_{ijk} is the bond angle between bonds ij and ik. Adjustable parameters γ, c, d and h have different meanings: the parameter c describes the strength of the angular effect; the parameter d determines the degree of dependence on the sharpness of the angle and the parameter h expresses the angular function's minimum.

To simulate high-energy events, it is necessary to improve the potential over its original form. For r reaching zero in the repulsive part, the energy should be varied according to the Ziegler-Biersack-Littmark (ZBL) universal screening function and the Coulomb potential [51]:

$$\tilde{V}_{ij} = f(r_{ij})V_{ij} + [1 - f(r_{ij})]V_{ij}^{ZBL} \tag{2.30}$$

here, V is the original potential, V_{ZBL} is the universal repulsive (ZBL) potential that can be described as below [53]:

$$V^{ZBL} = \frac{1}{4\pi\varepsilon_0}\frac{Z_i Z_j e^2}{r}\phi\left(\frac{r}{a}\right) \tag{2.31}$$

with $a = \frac{0.8854a_0}{Z_1^{0.23} + Z_2^{0.23}}$, $a_0 = 0.529\,\mathring{A}$ (Bohr radius),

$$\phi(x) = 0.1818e^{-3.2x} + 0.5099e^{-0.9423x} + 0.2802e^{-0.4028x} + 0.02817e^{-0.2016x} \tag{2.32}$$

and $f(r)$ is defined as the Fermi-like function that links smoothly the ZBL part with the original part. Parameter b_f is considered to control the "sharpness" of the transition and r_f indicates the cut-off distance for the ZBL potential. The function $f(r)$ is then written as:

$$f(r) = \frac{1}{1 + e^{-b_f(r - r_f)}} \tag{2.33}$$

In order to construct the potential by optimizing the parameters by reffering DFT energy database, a number of structures including the configurations where one or two carbon atoms are placed at an iron site (substitution), interstitial sites (at O-site or T-site) and trapped at iron vacancy of 3x3x3 supercell of BCC iron are calculated by DFT calculations. The parameters of the Fe-C classical potential are fitted by using the Genetic Algorithm which are illustrated in Table 2.

Table 2. Optimal iron-carbon potential parameters. The parameters for pure iron and pure carbon interactions are taken from previous works[50].

Parameters	**Fe-Fe**	**C-C**	**Fe-C**
S	2.0693	1.22	1.13068
B	1.4	2.1	1.63514
D_0	1.5	6.0	13.13087
r_0	2.29	1.39	0.98468
R	3.15	1.85	2.58980
D	0.2	0.15	0.29680
Γ	0.0116	0.0002	0.04200
C	1.2899	330.0	0.00730
D	0.3413	3.5	0.03530
H	0.26	−1.0	−0.01170
r_f	0.95	0.6	1.13470
b_f	2.9	8	5.41240

2.4. Method of analysis

2.4.1. Dissolution and Segregation energy

Dissolution energy of C in Fe configurations is calculated by following equation:

$$E_{dis} = E_X^{mFe+C} - E_X^{mFe} - \mu_C \qquad (2.34),$$

where X distinguishes the kinds of defects such as GB, vacancy, and dislocation.

The difference between dissolution energy of C in the defect configuration (X) and the one in pure bulk α-Fe is indicated as segregation energy (E_{seg}), which is calculated as,

$$E_{seg} = E_{dis}^{X} - E_{dis}^{bulk} = (E_X^{Fe+C} - E_X^{Fe} - \mu_C) - (E_{bulk}^{Fe+C} - E_{bulk}^{Fe} - \mu_C)$$

$$= (E_X^{Fe+C} - E_X^{Fe}) - (E_{bulk}^{Fe+C} - E_{bulk}^{Fe}) \quad (2.35)$$

where E_X^{Fe+C} and E_{bulk}^{Fe+C} represent the total energy of the supercell of the X defected iron configuration containing C and the total energy of bulk Fe with C located at the O-site, respectively. E_{bulk}^{Fe} and E_X^{Fe} are the total energy of bulk Fe without C and the total energy of the defected one, respectively.

2.4.2. Voronoi volume and coordination number

In order to determine the possible segregation sites of C in α-Fe matrix, we analyze the geometry of the defect systems. We assume that C atoms can form chemical bonding with surrounding Fe atoms. Chemical bonding is related to the coordination number, which is defined as the number of neighbour Fe atoms within a cut-off radius of 2.5Å from the C atom. It is noted that the lattice constant of α-Fe $a_{\mathbf{Fe}}$ is 2.8886Å obtained by using the Fe-C Tersoff potential. Hence, within the cut-off distance, the coordination number of C at O-site is 6 in α-Fe.

The mechanical distortion is estimated by considering the Voronoi volume and shortest bond length between C and Fe. The relation of C segregation sites and local atomic structure is also discussed from the view point of free space around C. For this purpose we construct Voronoi cell constructed by neighbouring Fe atoms around C (Fig. 2-2). The relation of C segregation sites and local atomic structure is also discussed from the view point of free space around C. For this purpose, the construction of Voronoi cell surrounding C is performed and taken into account for the discussion. For the calculations of the Voronoi volume associated with C atom, the external library Voro++ is used [54]. This external library is integrated in and implemented directly from the Large-scale Atomic/ Molecular Massively Parallel Simulator (LAMMPS)[55] code. The details of construction of Voronoi cell which specifies the Voronoi volume is as

follows: For a given set of three-dimensional points corresponding to the coordinates of Fe and C in the simulated supercell, the Voronoi cell of a particular point in this set is determined as a convex irregular polyhedron, the faces of which are the perpendicular bisecting planes of that point with its neighbors. Following this definition, any point located inside an atom's Voronoi cell is closer to that atom than any other one.

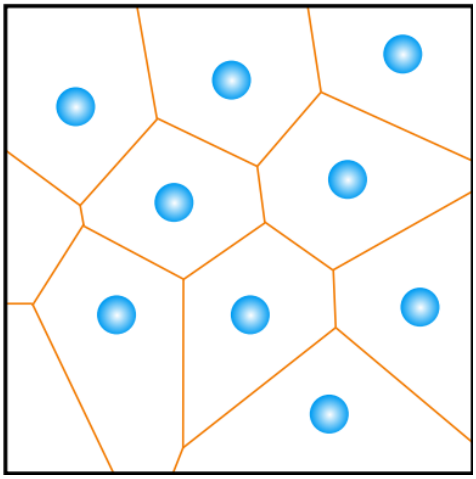

Fig. 2-1. Voronoi volume construction. The orange lines are the perpendicular bisectors between neighbouring particles.

CHAPTER 3. RESULTS AND DISCUSSION

3.1. Point defect

For the simulation, the system of a 5x5x5 supercell α-iron with 249 iron atoms containing single vacancy was studied. The interaction of C and vacancy with different C-V distances is investigated by using the Large-scale Atomic/ Molecular Massively Parallel Simulator (LAMMPS) [55] code.

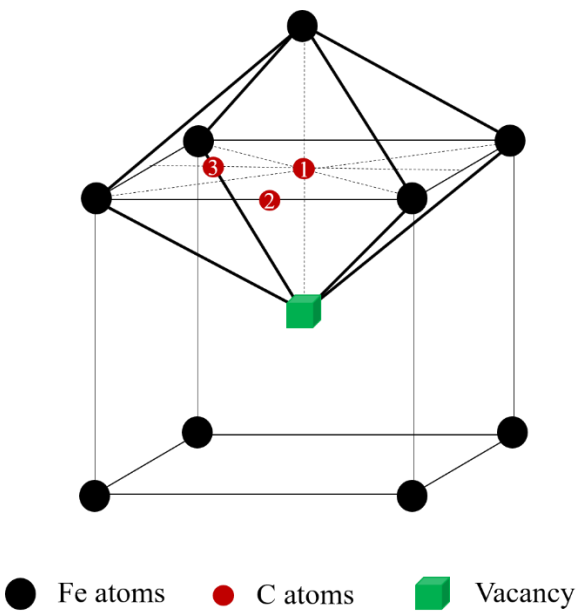

Fig. 3-1. C located at O-site in 1,2 positions and T-site in 3 position in Fe-V system.

The positions of C at O-site and T-site around V are illustrated in Fig. 3-1, in which C is located at the first nearest neighbour (1NN) and the second nearest neighbour (2NN) O-site, and 1NN T-site from the vacancy. Moreover, in order to consider the interaction distance between vacancy and carbon, some reasonable positions of carbon around vacancy site were considered. It is noted that the most

stable position of C in α-Fe is at the O-site [10, 49]. In Fig. 3-2, the location of carbon at different O-sites such as P1, P2, P3, P4, P5, P6, P7 are shown. Among them, the nearest position from vacancy is P1, next is P2 and so on.

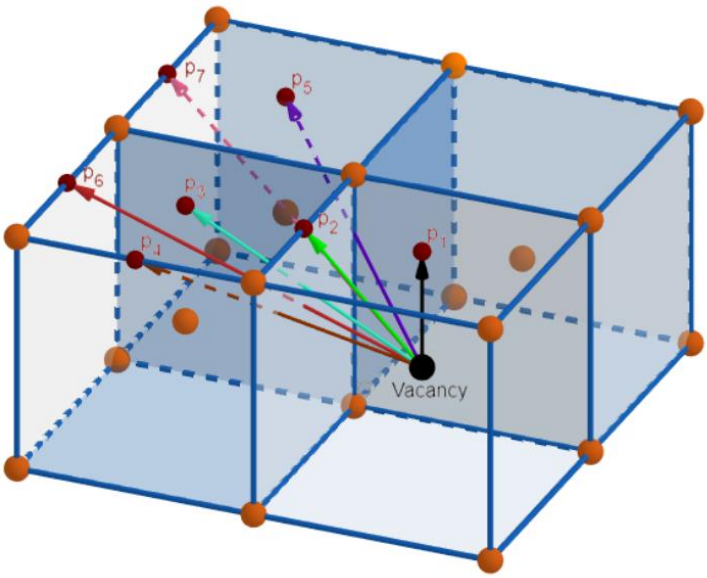

Fig. 3-2. Positions of carbon at O-site around iron vacancy. Orange balls present Fe atoms.

The interaction of C with vacancy is estimated based on the segregation energy of C which is defined in Chapter 2. Possible segregation sites of C are analysed by considering the correlation between segregation energy and local atomic structure factors.

Table 3. The segregation energy of C in O-site and T-site. $d_{C\text{-}V}$: Carbon vacancy distance Voronoi volume of C in O-site in perfect α-Fe: 7.05 Å^3

Configuration	$d_{C\text{-}V}$ (Å)	E_{Seg} (eV)	Voronoi volume (Å^3)	Shortest bond length (Å)	Coordination number
1NN O-site (P1)	1.055	-0.393	9.996	1.924	5
2NN O-site (P2)	2.032	0.098	9.228	1.773	5
P3	3.254	-0.132	7.01	1.777	6
P4	3.512	-0.416	7.06	1.793	6
P5	4.325	-0.085	7.06	1.787	6
P6	4.567	-0.086	7.06	1.787	6
P7	5.425	0.042	7.06	1.785	6

Due to the interaction between C and vacancy, C prefers to locate at the 1NN O-site and it shows negative segregation energy E_{Seg}=-0.393 eV which is quite in good agreement with the previous DFT calculations (-0.44 eV[10], -0.52 eV[56], -0.56 eV[57]). C located at P1 and P4. For P1 case, it is easy to find that this position will be stable because C atom is located right beside the vacancy, in the region where there is much of space for C to reside. While in the case of P4, the stability of C can be explained as follows: Due to the present of vacancy, 8 Fe atoms in the conventional BCC cell containing the vacancy at center will move toward the vacancy. Because of these displacements of 8 Fe atoms, the distance between two Fe atoms on the left- and right- hand sides of P4 (Fig. 3-2) is stretched, creating more free space for C to occupy. In fact, this explanation can

also be applied for P2 case. As it can be seen in Fig. 3-2, C atom located at P2 is expected to be stable because this position is the second nearest point to the vacancy compared to P1. However, Table 2 shows that this is not the case as the segregation energy of P2 point is the most positive one (most unstable). This is due to the displacement of Fe atoms mentioned above, leading to the shrinking of Fe-Fe distance aligning with P2. As a result, the free volume surrounding P2 is reduced, making it a disfavoured site for C to move into. To figure out the clear relation between interaction of C in defect BCC Fe and local atomic structure, the grain boundary and dislocation defects will be discussed in the sections below.

3.2. Grain boundary (GB)

3.2.1. Model of grain boundary

In the present simulations, we assume periodic boundary conditions, namely, atomic structure of STGBs is simulated by using supercell. For each STGB, corresponding supercell is generated by GBstudio software.[58] In this study, 9 structures of α-Fe <110> STGBs with the range of misorientation angle of 38.9˚-153.5˚ are considered. The unit-cell sizes of STGBs configurations before relaxation are provided in Table 3. The translation vectors $\boldsymbol{a_0}, \boldsymbol{b_0}$ and $\boldsymbol{c_0}$ define the supercell and are used for the DFT calculations. The rotation axis of the STGBs, namely <110> direction of BCC structure, is parallel to $\boldsymbol{b_0}$ and its length is $\sqrt{\mathbf{2}}\boldsymbol{a_{Fe}}$ where $\boldsymbol{a_{Fe}}$ is the lattice constant of BCC Fe. The directions of two perpendicular axes $\boldsymbol{a_0}$ and $\boldsymbol{c_0}$ and their lengths are also indicated in Table 3. $\boldsymbol{a_0}, \boldsymbol{b_0}$ defines the GB plane and $\boldsymbol{c_0}$ defines the thickness twin grains perpendicular to the GB plane. The distance of two adjacent STGBs is $\frac{\boldsymbol{c_0}}{\mathbf{2}}$.

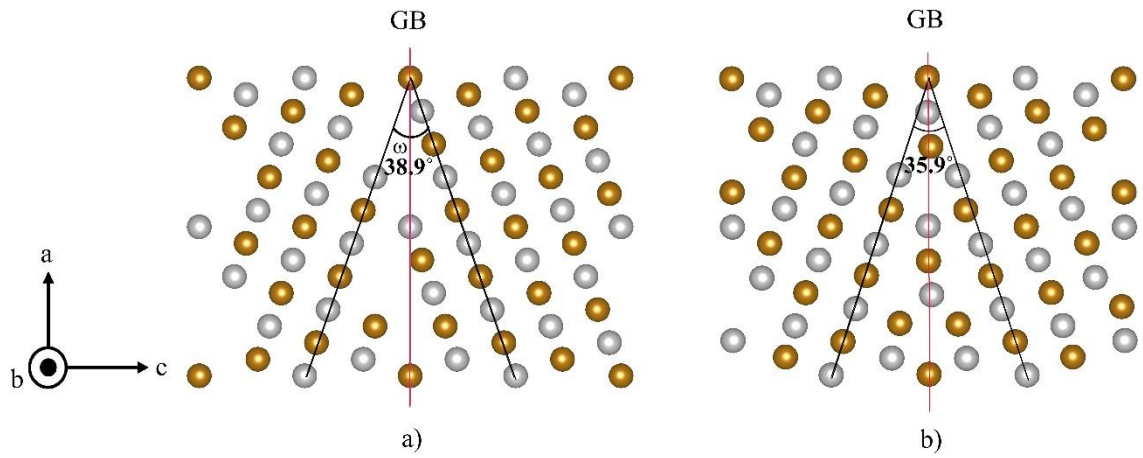

Fig. 3-3. Grain boundary structures of a) modified Σ9(221)38.9˚ STGB and b) its optimized structure. The grain boundary is perpendicular to c-axis. Orange and gray spheres represent Fe atoms lying on two adjacent atomic layers along rotation axis (b - axis)

The information of the supercells of the STGBs used for the simulations with classical interatomic potentials is shown in Table 4. The GB plane is constructed by two vectors $\boldsymbol{N_1 a_0}$ and $\boldsymbol{N_2 b_0}$ (where, $\boldsymbol{N_1}$ **and** $\boldsymbol{N_2}$ are integers) by using $\boldsymbol{a_0}, \boldsymbol{b_0}$ defined in Table 3 for each case. The width of twin is $\boldsymbol{c}$ and also indicated in Table 4. Among the considered STGBs, the simplest GB is Σ3(112) with misorientation of 109.5˚ which is well known as a twin GB configuration with [112] Miller index of grains. In other configurations with higher coincidence site lattice Σ values, the structure of GB becomes more complex. For example, in Σ9(221) GB, some Fe pairs come too close with each other. In such cases, to simplify the calculation, some Fe atoms are removed as shown in Fig. 3-3a). The resulting STGB structure becomes asymmetric but by relaxing the structure, the symmetric arrangement is recovered for most cases, as shown for the case of Σ9(221) GB in Fig. 3-3b).

All the calculations with classical interatomic potentials are carried out by using the LAMMPS. In addition to the new Tersoff/ZBL interatomic

potential[49,50], the calculations are also performed in conjunction with the EAM potential[31] for comparison. To avoid strong interaction of two adjacent GBs, calculations using classical potentials are performed with large cells of STGBs. For some typical cells of STGBs with small number of atoms (the their sizes are listed in Table 3), we performed DFT calculations in order to confirm the reliability of presently constructed Tersoff/ZBL potential. Our DFT calculations were performed by using the spin-polarized version of the Vienna Ab initio Simulation Package (VASP) [59].The Perdew-Burke-Ernzerhof (PBE) functional based on the generalized gradient approximation (GGA)[60, 61] was employed for the electronic exchange-correlation interaction. The projector-augmented-wave (PAW) pseudopotential was taken from PAW database where the 3d, 4s states of Fe are treated as valence states. An energy cut-off of 450 eV is used for all calculated systems, and all relaxation calculations are performed until a residual force of 10^{-2} eV/Å is achieved. The calculated lattice constant $\boldsymbol{a_{Fe}}$ of BCC Fe is 2.84Å with the k-point mesh of 15×15×15.

3.2.2. Grain boundary energy

In order to examine the stability of GBs, grain boundary energies (GBEs) with and without C were calculated by the following equation:

$$\gamma_{GB} = \frac{E_{GB}^{mFe+nC} - m\mu_{Fe} - n\mu_C}{2A} \quad (3.1),$$

where E_{GB}^{mFe+nC} is the total energy of the supercell of the STGBs systems containing m Fe atoms and n C atoms, and μ_{Fe}, μ_C are the chemical potentials of Fe atom in perfect BCC structure and C in diamond, respectively. *A* is the area of calculated STGB.

In GBE calculations, the periodic boundary conditions along three directions are applied. Hence, *2A* is used in *Eq*. (3.1) to indicate two symmetric

GB interfaces for each calculated supercell. Firstly, we assume there is no C in the system, namely n = 0, and calculated values of γ_{GB} by the DFT and the classical interatomic potentials are compared. The obtained values of γ_{GB} are compared and illustrated in Fig. 3-4. For both cases, the STGB structures are fully optimized. Both of the present DFT and classical force-field calculations confirm that the most stable STGB is ∑3(112), which is in good agreement with previous studies [32, 62, 35-38] The ∑9(221) is predicted as the most unstable STGB among the presently calculated ones. The results of classical force-field calculations using the new Tersoff/ZBL potential reproduce DFT results reasonably as compared with those obtained by the EAM and Johnson potentials. Therefore, the present Tersoff/ZBL interatomic potential has shown to be a good force-field for calculating complex GBs system, and we use the potential for all of the following simulations.

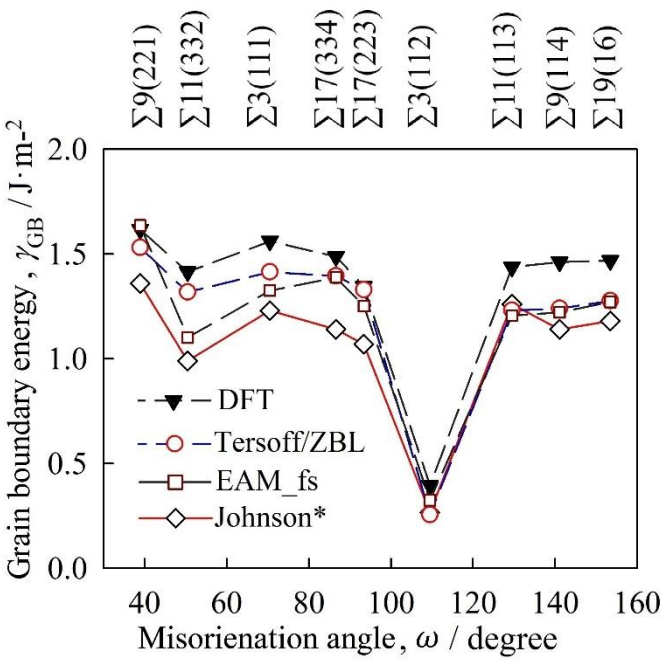

Fig. 3-4. Grain boundary energy as a function of misorientation angle. The GBE values calculated by Johnson potential are taken from previous study (ref[30])*

The stability of grain boundaries can be explained by considering free volume of grain boundary. The free volume of GB indicates the excess volume around Fe atoms constructed by establishing GB per GB area comparing to volume of perfect BCC Fe (eq 3.2).

$$\Omega_{GB} = \frac{V_{GB}^{mFe} - m\upsilon_{Fe}}{2A} \tag{3.2}$$

where Ω_{GB} is free volume of GB, V_{GB}^{mFe}, υ_{Fe} are volume of GB system containing m Fe atoms and volume of a Fe atom in perfect bulk BCC Fe, respectively. A is area of GB.

The free volume imply the excess volume due to the formation of grain boudary comparing to prefect α-Fe. The larger value of free volume corresponds to how large difference between GBs and perfect structures. The relation of GBEs and these free volumes is illustrated in Fig. 3-5. It can be seen that the smaller energy GBs correspond to the smaller free volume of these GB and vice versa.

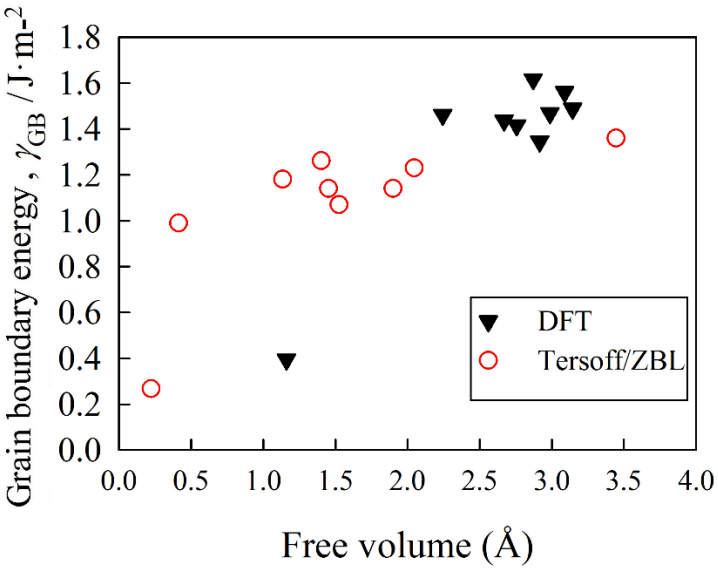

Fig. 3-5. The grain boundary energy as a function of free volume.

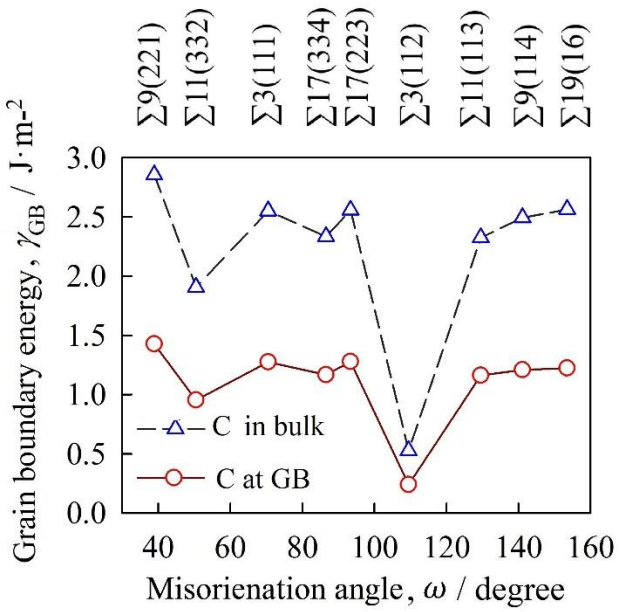

Fig. 3-6. Grain boundary energy of STGBs with C calculated by using classical interatomic potential. $\boldsymbol{\gamma_{GB}^{C}}$ *and* $\boldsymbol{\gamma_{GB}^{ref}}$ *values are indicated by red circles and blue triangles, respectively.*

Next, to determine the influence of C on the stability of STGBs, the GBEs (γ_{GB}^{C} and γ_{GB}^{ref}) of STGBs including one C (i.e., n = 1) are calculated and compared by using eq (1). Herein, the GBEs γ_{GB}^{C} are obtained by introducing C at the most stable position in GB. The areal concentration of C in GBs is shown in Table 4. The reference of GBEs (γ_{GB}^{ref}) was calculated for the configuration in which the C atom is inserted at the most stable position in bulk BCC Fe, which is about 2.2-4.4 nm away from the GBs. At these distances, the interaction of C with GBs is negligible, this means that C atom exhibits as in bulk BCC Fe while the GBEs in these cases are considered to be the same as in the case of no C (γ_{GB}). As shown in Fig. 3-6, generally the energy of STGBs is reduced by introducing C at GB comparing with C at a distance away from GB. In the ∑3(112) GB, carbon at GB is shown to have very small influence on the GBE. This is reasonable, because this GB is considerably stable and its local structure is similar to bulk Fe. On the other hand, C shows strong effect on other STGBs such as ∑11(332), ∑9(114),

and ∑19(116). They are basically unstable GBs and the local structures are very much different from the bulk Fe. Quantitative discussion between the stability of C and the local structure will be discussed later in section 3.2.3.

Table 4. Unit cell used for the DFT calculations on grain boundary energies of typical STGBs. Here, ω is misorientation angle, m is number of Fe in the unit cell. $\gamma_{GB}{}^{*}$ values are obtained from previous DFT studies.

STGB Configuration	**Unit cell size**			**Direction**	$\boldsymbol{\omega}$ (°)	$\boldsymbol{m}$	**k-point mesh**	$\boldsymbol{\gamma_{GB}}$	$\boldsymbol{\gamma_{GB}}^{*}$
	$\lvert\boldsymbol{a_0}\rvert$ **(nm)**	$\lvert\boldsymbol{b_0}\rvert$ **(nm)**	$\lvert\boldsymbol{c_0}\rvert$ **(nm)**	$\boldsymbol{a_0}$ $\boldsymbol{b_0}$ $\boldsymbol{c_0}$				(eV· Å^{-2})	J· m^{-2}
Σ9(221)	1.21	0.40	1.72	<$\bar{1}$14> <110> <2$\bar{2}$1>	38.9	64	3×10× 3	0.101	1.71[35]
Σ11(332)	0.95	0.40	2.69	<$\bar{1}$13> <110> <3$\bar{3}$2>	50.5	84	5×11× 2	0.089	1.49[35]
Σ3(111)	0.70	0.40	1.99	<$\bar{1}$12> <110> <1$\bar{1}$1>	70.5	48	6×10×2	0.098	1.61[35] 1.57[36] 1.52[37]
Σ17(334)	1.18	0.40	3.34	<$\bar{2}$23> <110> <3$\bar{3}$4>	86.6	28	3×11×1	0.093	
Σ17(223)	1.67	0.40	2.36	<$\bar{3}$34> <110> <2$\bar{2}$3>	93.4	28	2×6×1	0.084	
Σ3(112)	0.49	0.40	2.81	<$\bar{1}$11> <110> <1$\bar{1}$2>	109.5	48	8×10×2	0.026	0.43[35] 0.34[37] 0.47[38]
Σ11(113)	1.34	0.40	1.90	<$\bar{3}$32> <110> <1$\bar{1}$1>	129.5	80	3×11×2	0.090	
Σ9(114)	0.86	0.40	2.43	<$\bar{2}$21> <110> <1$\bar{1}$4>	141.1	68	5 ×10×3	0.091	
Σ19(116)	1.25	0.40	3.53	<$\bar{3}$31> <110> <1$\bar{1}$6>	153.5	40	4×10×1	0.092	

Table 5. Supercells used for the calculations using Tersoff/ZBL potential on various <110>STGBs.. The supercell size is indicated by using vectors $\boldsymbol{a_0}$ and $\boldsymbol{b_0}$ defined in Table 3. Grain boundary energy, segregation energy of C and Voronoi volume of C are also summarized.

	Supercell size $N_1a_0 \times N_2b_0 \times c$			m	ω (°)	γ_{GB} [(eV· Å^{-2})]	**Areal C conc. (1/nm^2)**	γ_{GB}^{C} (eV· Å^{-2})	E_{seg} (eV)	Voronoi volume of C (Å^3)
	N_1	N_2	c (nm)							
Σ9(221)	3	6	8.61	6336	38.9	0.095	0.115	0.089	-1.78	8.39
Σ11(332)	5	5	13.46	10900	50.5	0.082	0.102	0.060	-1.46	8.22
Σ3(111)	10	10	9.93	24000	70.5	0.088	0.035	0.080	-1.16	8.38
Σ17(334)	5	5	11.82	16800	86.6	0.087	0.058	0.073	-0.76	8.41
Σ17(223)	5	5	16.73	16800	93.4	0.083	0.083	0.080	-0.56	7.86
Σ3(112)	6	6	8.46	5184	109.5	0.016	0.137	0.015	-0.53	7.50
Σ11(113)	5	5	9.52	10800	129.5	0.077	0.073	0.072	-1.10	7.94
Σ9(114)	5	5	12.16	8900	141.1	0.078	0.014	0.075	-1.09	7.90
Σ19(116)	5	5	17.67	18800	153.5	0.080	0.078	0.076	-1.60	8.01

3.2.3. Segregation sites

The segregation sites of C are determined by examining the landscape of the dissolution energy (E_{dis}) of C in the GB systems. In this calculation, a single C is inserted on a middle plane of two Fe layers corresponding to [022] plane in the bulk BCC structure. This plane includes a set of O-sites, the most preferable location of C. On this plane, a 100x100 mesh lying along two lattice vectors are set up and the dissolution energy of C for each mesh point is estimated by optimizing the structure with C position kept fixed. In Fig. 3-7, the scanning planes and dissolution energy landscapes of two typical STGBs, namely, the most stable ∑3(112) STGB (Fig. 3-7a) and the most unstable one, ∑9(221) STGB (Fig. 3-7b) are illustrated. Here, the darker color (dark blue) reflects the higher energy area in which C is less preferred, whereas the lighter area (red) illustrates the favourable location of C. As can be seen that the unstable area of C is the area close to Fe atoms, indicating the strong repulsive interaction between C and Fe atoms. The lighter area of GB planes indicates an attractive source of C compared to the one in the distant GB. Besides, possible positions of C are found at O-sites in the distant GB area. Similar calculations are also performed for the other STGBs. All obtained results confirm that C is preferably located at the GB plane considered in the present study.

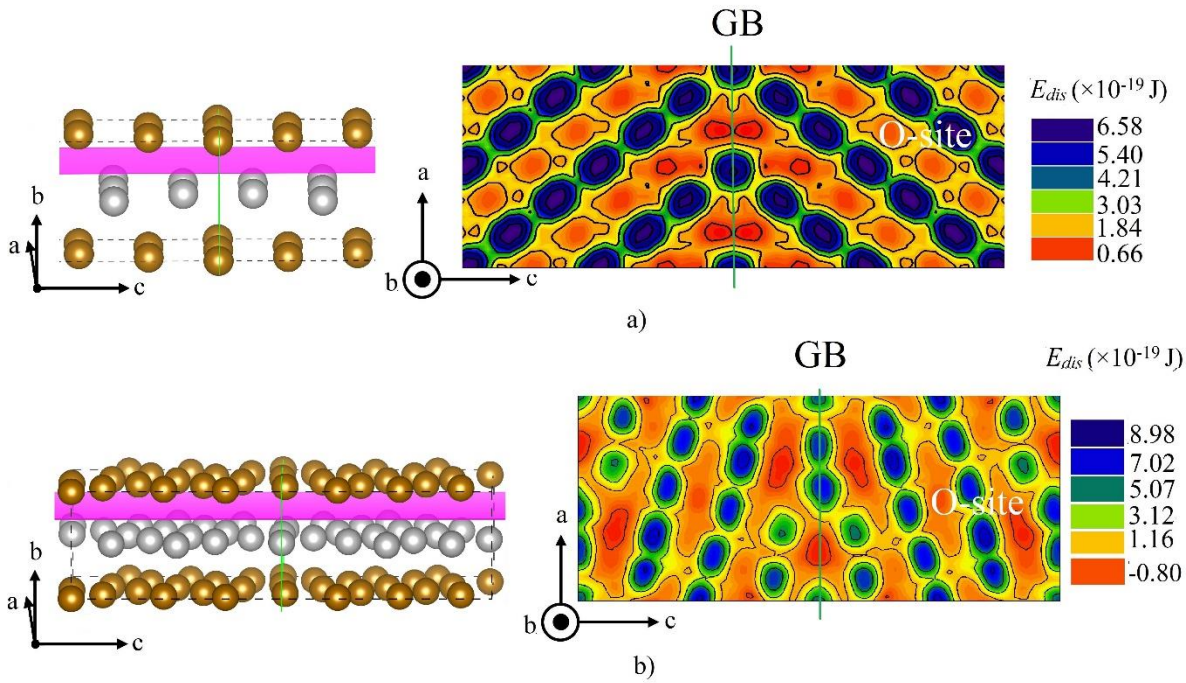

Fig. 3-7. Scanning planes (colored in pink on the left-hand side sub-figures) and dissolution energy landscapes (right-hand side sub-figures) of FeC systems of a) Σ3(112) STGB and b) Σ9(221) STGB. The location of GB is indicated by green dashed line.

3.2.4. Segregation energy

In order to figure out the behaviour of C, the E_{seg} is calculated for various STGBs and the results are summarized in Table 4. For all of the STGBs considered in this thesis, the segregation energies E_{seg} are found to be negative, which indicates a strong segregation tendency of C atoms to the GBs from the bulk region. Among the considered STGBs, the ∑3(112) GB has the highest segregation energy of -0.53 eV, and the ∑9(221) GB has the lowest E_{seg} of -1.78 eV. In order to discuss the origin of difference in segregation energy from the view point of the local atomic structure, we focus on the free volume defined by neighboring Fe atoms around C.

For this purpose, we define Voronoi cell around C as free volume. In Fig. 3-8, the correlation between the Voronoi volume of C and its E_{seg} is shown. In the figure, C is assumed to be located not only on the GB but also off the GB plane for each system. It is clearly observed that there is a negative correlation between them, namely the larger free volume STGBs is, the more negative E_{seg} is predicted. The negative correlation was not clear in the previous DFT calculation [32] due to the limited number of calculated GBs, but the trend of the most stable position of C at GBs is consistent to the present results.

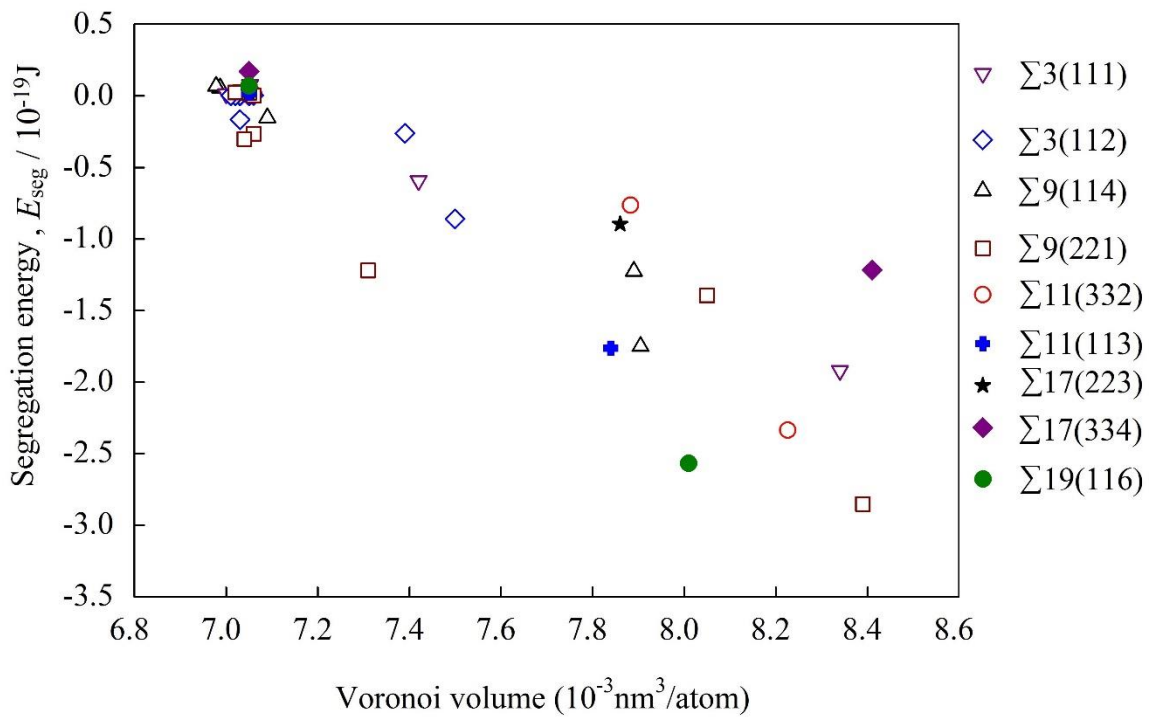

Fig. 3-8. The relationship between segregation energy and Voronoi volume of C in different STGBs. In this plot not only the C on the GB plane but also the C off the GB plane are included.

In order to extend the above discussion, we calculate E_{seg} as a function of distance between C and GB plane for STGBs, namely ∑3(112), ∑3(111), ∑9(221), ∑9(114), and ∑11(332). At the same time, for each position of C, the Voronoi volume is calculated. For this procedure, a single C atom is inserted at the stable positions which are predicted based on the energy landscapes obtained in Section 3.2.3. The results are shown in Fig. 3-9. E_{seg} takes the lowest value when C is placed at the GB plane ($d_{\text{GB-C}}$ = 0) then gradually increases and approaches zero as C is moved far away from the GB plane. The distance dependence of E_{seg} corresponds very well with the change of the Voronoi volume of C, namely the Voronoi volume reaches to the highest value when C located at the GB plane and from there the lowest E_{seg} is obtained. A gradual decrease of Voronoi volume is found when increasing the distance from C to the GB, $d_{\text{GB-C}}$. The minimum of Voronoi volume of around 7.0×10^{-3} nm^3 is obtained when C is located in distant GB. This is almost the same to the value of C in bulk Fe (7.05×10^{-3} nm^3). By considering the effect of the Voronoi volume to the behaviour of C in various STGBs, it can be concluded that the GB creates open space for C occupation, resulting in C being strongly trapped by the GB.

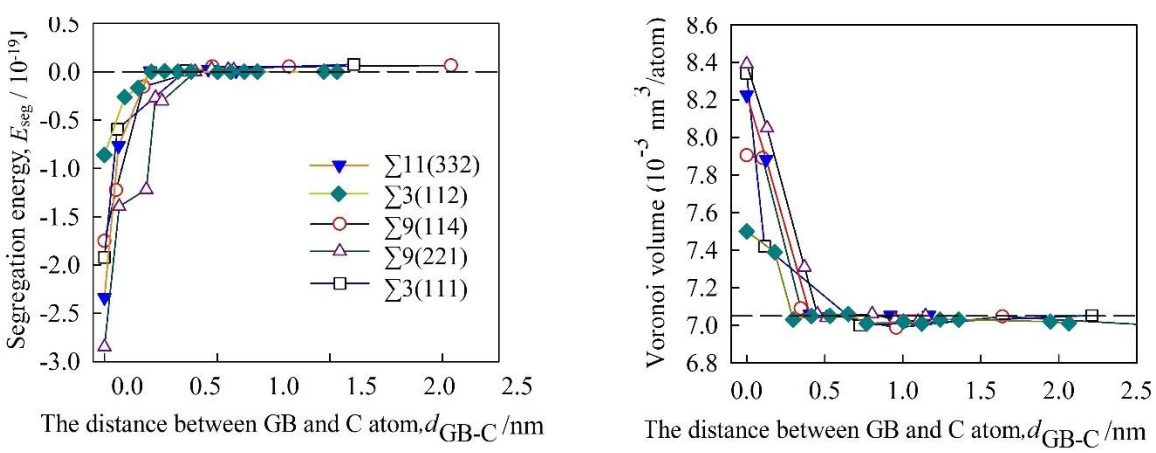

Fig. 3-9. The segregation energy of C (left) and Voronoi volume (right) as functions of the distance between GB and C. The horizontal dashed line at the

bottom of the right-hand side sub-figure indicates the Voronoi volume of C located at O-site in BCC bulk iron.

In the most stable GB configuration ∑3(112), E_{seg} is small but we can still find the anti-correlation between E_{seg} and the Voronoi volume of C. As already shown in Fig. 3-9, this behaviour is also clear for the other GBs. It is suggested that the anti-correlation between Voronoi volume around C and the segregation energy is general for Fe-C systems. Experimental confirmation of this finding is desirable. For ∑3(112) GB, a small difference in E_{seg} between the position on the GB plane and distant GB is shown, it means that such GB behaves as a weak attraction to C. It was observed that a significantly lower excess of C is detected in the experimental study for special stable ∑3 and ∑5 GBs.[16)] On the contrary, in the case of ∑9(221) configuration, C is strongly trapped at the GB plane when compared to other locations. The strong interaction of Fe-C in the GB plane prevents the difusion of C to the bulk. Therefore, a high solubility of C can be expected in Fe matrix by controlling the inclination of GB planes.

It can be concluded that the GBs exhibit stronger attraction to C than the other point defects in the BCC Fe matrix, and the lowering of the GB energy due to the existence of C might partly contribute to the strengthening effect of C. [32]

3.3. Dislocation

In the present simulations, 5 different edge dislocation configurations are constructed by using Atomsk code [63]. They are: two edge dislocations with the Burgers vector ***b*** <111> and glide planes (110) and (112), two with the

Burgers vector ***b*** <100> and glide planes (011) and (010), and the one dislocation with ***b*** <110> and (110) glide plane. The translation vectors which create dislocation configurations and magnitude of Burgers vectors are listed in Table 6. L_x, L_y, L_z are length of translation vectors which create the basic unit cell of edge dislocation models. The edge dislocation model (a three-dimensional model) in the form of a supercell with periodic boundary condition is illustrated in Fig. 3-10. A supercell containing 4 dislocation cores (quadrupole model) has been investigated. A quadrupole model of dislocations can be constructed by two pairs of dislocation cores with opposite sign. Herein, number of atomic layers are the same in the upper/lower parts and the middle part of the supercell. In the supercell of quadrupole model, four dislocation cores are inserted: two with positive Burgers vectors at the reduced coordinated (0.251, 0.251) and (0.749, 0.749), and two with negative Burgers vectors at (0.251, 0.749) and (0.749, 0,251) with the X axis corresponding to Burgers vector, dislocation line lying along Y axis, and Z axis normal to glide plane. D is the distance of two adjected dislocation cores.

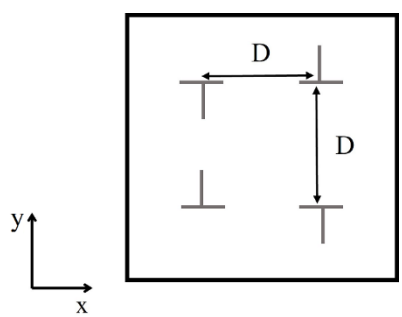

Fig. 3-10. Quadrupole dislocation model. D corresponds to the distance of two adjacent dislocation cores.

Table 6. Structure of edge dislocations considered in the present study. L_x, L_y, L_z are basic unit cell size which create dislocation models, and $|\boldsymbol{b}|$ is the magnitude of Burgers vector. For each dislocation configuration, glide plane is perpendicular to slip direction.

Configuration	Burgers vector $\boldsymbol{b}$	Slip direction	Dislocation line	Basic unit cell		
				$L_x/\|\boldsymbol{b}\|$ (nm)	L_y (nm)	L_z (nm)
<111>{110}	½<111>	$<1\bar{1}0>$	$<11\bar{2}>$	0.25	0.41	0.71
<111>{112}	½<111>	$<11\bar{2}>$	$<1\bar{1}0>$	0.25	0.71	0.41
<100>{010}	<100>	<010>	<001>	0.29	0.29	0.29
<100>{011}	<100>	<011>	$<0\bar{1}1>$	0.29	0.41	0.41
<110>{110}	<110>	$<1\bar{1}0>$	<001>	0.41	0.41	0.29

3.3.1. Dislocation energy

The supercell size of quadrupole dislocations is chosen by considering the change of the formation energy of the dislocation $\Delta E_{dislocation}$ when increasing the size of the supercell. $\Delta E_{dislocation}$ is estimated by following equation:

$$\Delta E_{dislocation} = \frac{E_{dislocation}^{mFe} - m\mu_{Fe}}{4L} \quad (3.4),$$

where $E_{dislocation}^{mFe}$ is the total energy of the supercell containing 4 dislocations with m Fe atoms and μ_{Fe} is the chemical potential of Fe atom in the perfect BCC structure. It is obtained after optimizing the supercell volume and atomic positions. L is the length of dislocation line in the supercell. Since the quadrupole model has 4

dislocations in one supercell, we have factor 1/4 in eq (1). The definition in eq (1) implies that, the smaller $\Delta E_{dislocation}$, the more stable dislocation is. In this work, the stability of edge dislocations is figured out by comparing the dislocation energy $\Delta E_{dislocation}$ with supercell size dependence being taken into account. The size of supercell is gradually increased in both x and y direction which corresponds to increasing the distance of two adjacent dislocation cores (D). The dependence of $\Delta E_{dislocation}$ and D is illustrated in Fig 3-11. The dislocation energies of edge dislocations rise continuously with the increasing of the distance D. The size dependence of the dislocation energy shows logarithmic-like behavior which is consistent to the prediction of elastic theory, where the energy of an edge dislocation increases logarithmically as a function of distance from the dislocation core.) Among considered edge dislocations, it is found that ½<111>{110} edge dislocation has the smallest $\Delta E_{dislocation}$ and ½ <111>{112} dislocation is the second smallest one. This is to say, the most stable dislocation is ½<111>{110} and the second stable dislocation is ½ <111>{112}, which are consistent with the conclusion from experimental observation. [33,34)] The dislocations with Burgers vector <100> and gilde planes {010} and {011} are shown to be less stable than the ones with Burgers vector ½<111>, with a small energy diference. This might explain the transformation of ½<111> dislocation loop to <100> dislocation in previous theoretical studies and experiment observation at high temperature.[35-37)] In present dislocations, the $\Delta E_{dislocation}$ value of <110> dislocation is the highest one which is significantly different as compared to other dislocations, namely, it is the most unstable one from computational investigation. This result is consistent with the fact that this dislocation is not observed in experiments and known as unstable dislocation in contrast to the case of FCC metals. The order of stability obtained by the present calculations can be reasonably explained by the elastic theory which predicts that the dislocation energy is proportional to $|\boldsymbol{b}|^2$ (Table 6).

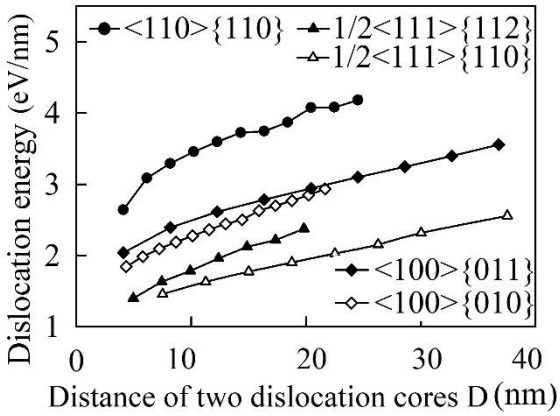

Fig. 3-11. Dislocation energy as a function of distance D between two adjacent dislocation cores (proportional to the supercell size) of different dislocation configurations calculated by classical force-field method using the new Fe-C potential.

3.3.2. Carbon segregation in dislocation

The reliability of our newly-developed potential was examined in cases of carbon segregation at vacancy and grain boundary in BCC iron.[49,50,73] For the calculations of edge dislocation, this procedure is also considered by comparing the results calculated by our new potential to the results from previous DFT calculations. In previous study, the interaction of C with <100>(001) edge dislocation core was investigated using DFT calculation[70]. Because the limitation of number of atoms in DFT a cluster of Fe containing dislocation core was extracted from the optimized configuration of <100>(001) edge studied by using Finnis-Sinclair potential.

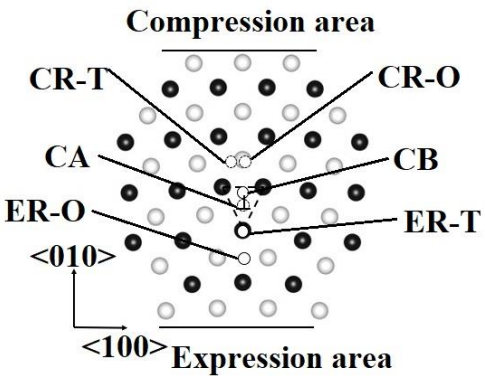

Fig 3-12. Atomic model of the <100>(010) edge dislocation core and different interstitial sites. Black and white balls represent Fe atoms in two adjacent planes (plane A and plane B, respectively) along <001> direction. Solid circles and dashed circles represent positions of C atom in plane A and plane B, respectively.

Here, the structure of Fe cluster, as shown in Fig. 3-12, is divided into two regions: a compression region (CR) and an expansion region (ER). The black and white balls represent Fe atoms in two adjajent planes along <001> direction (or dislocation line). To determine the interaction energy between C and dislocation

core, C is singly inserted into the center of plane A (CA, above dislocation core) and plane B (CB, under dislocation core), octahedral site in compression region (CR-O) and expansion region (ER-O), tetrahedral site in compression and expansion region (CR-T and ER-T, respectively). Similar to previous work, the periodic boundary condition is applied to the <001> direction while kept fixed along <100> and <010> directions. In addition, for the Fe-C system, some empirical interatomic potentials have already been implemented in LAMMPS. Therefore, to find out the advantages of our newly-developed Tersoff/ZBL potential, the calculations are also carried out by using other potentials, namely EAM [71)] and MEAM [72)]. In previous study [70)], the interaction of C and edge dislocation was discussed by using segregation energies. However, the definition of those segregation energies is different to our present study. To avoid confusion hereafter the segregation energies presented in ref. 70 is denoted as dissolution energy E_{diss} and expressed as follows:

$$\boldsymbol{E_{diss}} = \frac{\boldsymbol{E_b^{dop} - E_b^{clean}}}{\boldsymbol{N}} \qquad (3.5)$$ [38]

Where N is number of C atoms, $\boldsymbol{E_b^{dop}}$ and $\boldsymbol{E_b^{clean}}$ are binding energies of the C-doped system and clean system, respectively. The calculated dissolution energies E_{diss} for different C sites are listed in Table 7.

Table 7. Dissolution energy E_{diss} (eV) of carbon at different interstitial sites calculated by DFT (ref. 70) and other classical interatomic potentials.

	Core center		Compression region		Expansion region	
	CA	CB	CR-T	CR-O	ER-T	ER-O
Tersoff/ZBL	−7.61	−8.78	−7.34	− 7.63	−8.03	−7.69
MEAM	-6.97	−8.43	−6.69	-6.71	−6.92	-6.35
EAM	−5.69	−6.01	−3.13	−2.37	−3.57	−4.01
DFT[70]	−9.20	−9.84	−9.02	−9.04	−9.62	−9.22

By using Tersoff/ZBL potential, we can see that the most stable position of C around dislocation core is located in CB. This result is in good agreement with those obtained by other interatomic potentials and DFT. For the next stable site of C, our Tersoff/ZBL potential predicts ER-T site, which is also consistent with DFT calculation, while for EAM and MEAM potentials, the second most stable is found to be CA site. Overall, the values of E_{diss} calculated from Tersoff/ZBL potential are higher than DFT results by at most 1.68 eV, which is much lower than those obtained by MEAM (2.87 eV) and EAM (6.02 eV). The small discrepancy implies a better performance of our new potential for this specific Fe-C system as compared to other interatomic potentials. This is also complemented by the fact that the trend of dissolution energy reproduced by our potential agrees very well with the DFT calculations as compared to others (see Table 7).

½<111>(110) dislocation

Here, we consider the ½<111>{110} edge dislocation with Burgers vector ½<111> and glide plane {110}. For this dislocation, the glide plane is normal to $<\bar{1}10>$ direction and the dislocation line lies along $<11\bar{2}>$ direction. The dislocation model is created based on a basic unit cell of $L_x \times L_y \times L_z$ (Fig. 3-13 a). The dislocation system contains 151200 atoms.

The O-sites in α-Fe are located at the middle of edges or the centre of faces of BCC lattice which could be in <100>, <010>, or <001> directions corresponding to TDA(100), TDA(010), and TDA(001) sites (Fig. 5a). Here, TDA is an abbreviation for "tetragonal distortion axis" which indicates the largest distortion of lattice due to the insertion of C.[42, 33)] The position of C in different layers along $<11\bar{2}>$ direction is shown in Fig. 3-13 b. In Fig. 3.13 b, the Voronoi volume of Fe atoms around dislocation core is illustrated using a colour map and positions of C under consideration at different layers from the glide plane are shown. The value of Voronoi volume increases as the colour changes from red to blue. As we can see, the area above the dislocation core is more compressed while the area below the dislocation core is more expanded. The compression and expansion are reduced with moving away from the dislocation core. The C in the TDA(010) and TDA(100) located along 0.5 and 1.5 layers from the glide plane while the ones in the TDA(100) are right on the glide plane or along 1.0 and 2.0 layers.

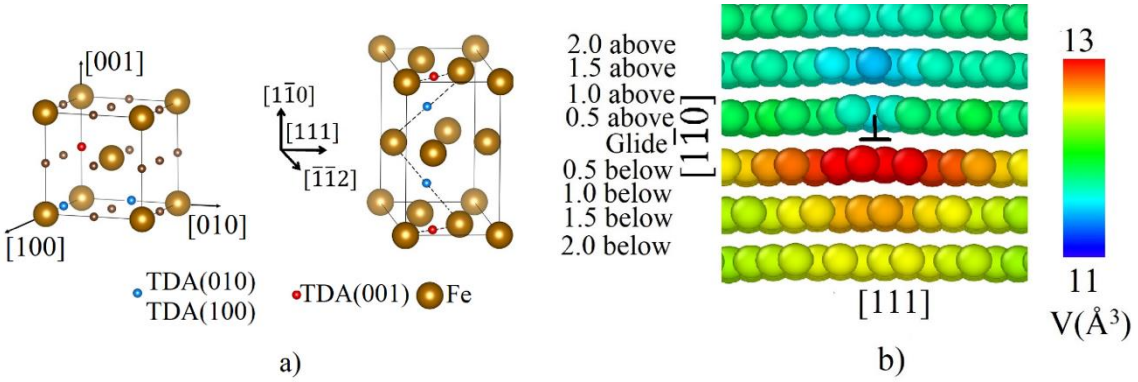

Fig. 3-13. a) BCC Fe and basic unit cell of Fe with the corresponding O-sites where C resides and b) The colour map of the Voronoi volume of Fe around the dislocation core and the positioning levels of C under consideration at different layers referring from the glide plane.

In Fig. 3-14, the segregation energies of C along TDA(001) and TDA(010) as functions of distance from C to the dislocation core (in unit of $\boldsymbol{a}_{\mathbf{Fe}}$) are shown. Results for the C segregation in TDA(001) are presented in Fig. 3-14 a and those in TDA(100) and TDA(010) are presented in Fig. 3-14 b. It can be seen that the C segregation in TDA(001) is highly symmetric for both sides of the dislocation core (Fig. 3-14 a). While, the asymmetry for C segregation is shown in Fig. 3-14 b for left- and right-side of the dislocation core, which can be explained by considering local atomic structure of iron. As shown in Fig. 3-13 a the octahedral geometry of the TDA(001) sites is symmetric along Burgers vector <111>, in contrast to those of the TDA(010) and the TDA(100) sites. This mainly contributes to the asymmetry of the local structures on two sides of the plane which is normal to the glide plane and contains the dislocation line. In both cases, the interaction between carbon and dislocation is weaker when C is located at a distance layer along <11$\bar{\mathbf{2}}$> direction from the glide plane. Based on the calculated segregation energy, strong interaction range between C and dislocation is within 5$\boldsymbol{a}_{\mathbf{Fe}}$ (about 1.44nm) for TDA(001) and 10$\boldsymbol{a}_{\mathbf{Fe}}$ (about 2.89nm) for TDA(010). When C atom is located far from the dislocation core, the E_{seg} values

approach to that of C in bulk BCC Fe. Considering the E_{seg} of C in different layers from the glide plane, interaction of C and dislocation is weaker in the layer which are distant from the glide plane. As shown in Fig. 3-14, C lying along the TDA(010) shows the lowest segregation energy of -1.11 eV at the dislocation core, which is lower than those obtained from Johnson and EAM potentials.[17,22] This is because of the different dislocation model and interatomic potential used in present study.

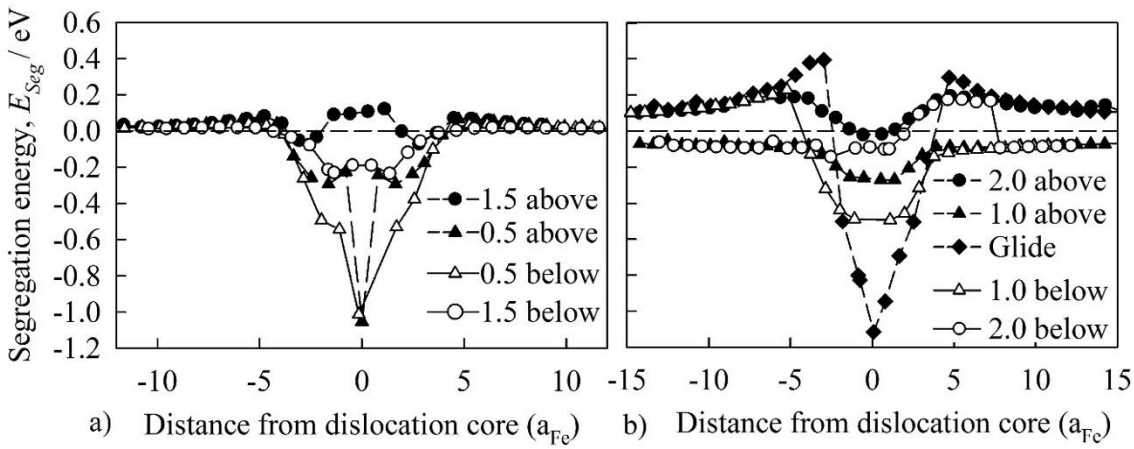

Fig. 3-14. Segregation energy of C in system containing ½<111>(110) edge dislocation with C at O-sites lying along a) TDA(001) and b) TDA(010) and TDA(100).

In Fig. 3-14 b, the segregation energies of C along TDA(001) as functions of distance from C to the dislocation core are shown. It can be seen that the dependence of segregation energy of C in this case is asymmetric at two sides of the dislocation core. This is mainly attributed to the asymmetry of the local structures on two sides of the plane which normal to the glide plane and containing the dislocation line.

½<111>(112) dislocation

The ½<111>{112} dislocation is characterized by Burgers vector ½<111> and glide plane {112} containing 180000 Fe atoms in calculation of C segregation. The positions of C at the O-sites are also considered along the TDA(100), TDA(010) and TDA(001) as in previous case. The calculated position-dependence of C segregation energy is plotted in Fig. 3-15. The figure shows the interaction between dislocation and C located along the TDA(001) (Fig. 3-15 a). The interaction is repulsive when C is on the right side of the dislocation line (<110> direction) and attractive if C is on the left side of the dislocation line. In contrast, the C lying along the TDA(010) and TDA(100) (Fig. 3-15 b) does not prefer to locate on the left side of the dislocation line which is qualitatively in agreement with previous study.[17)] The strong interaction range of C and ½<111>{112} dislocation is within 10 $\boldsymbol{a_{\mathrm{Fe}}}$ (about 2.89nm) for both TDA(001) and TDA(010). As shown in Fig. 3-15 b, C belonging to the TDA(100) shows the lowest segregation energy of -1.35 eV at the dislocation core. This energy is lower than the case of the ½<111>{110} dislocation, which is also observed in previous calculations.[17,22)]

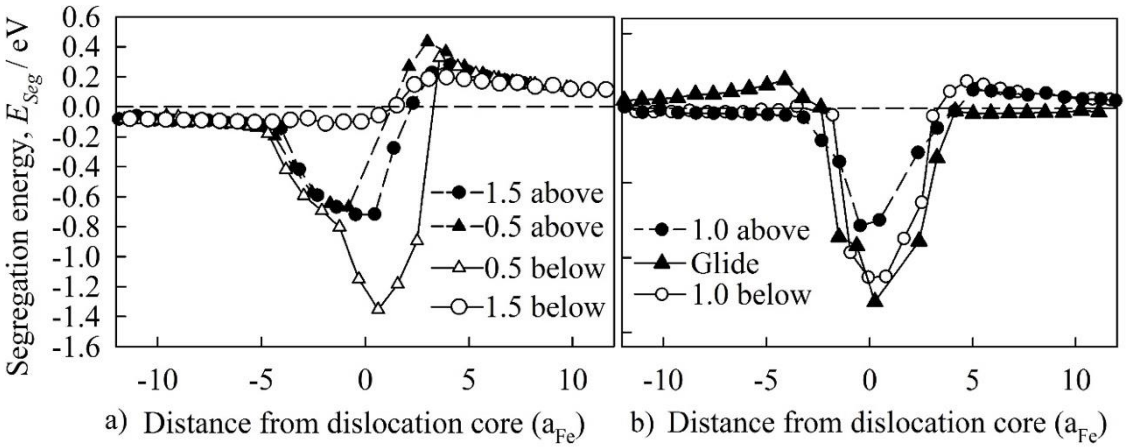

Fig. 3-15. Segregation of C in ½<111>(112) edge dislocation with one C in a) TDA(001) and b) TDA(010) TDA(100).Segregation energy of C in system containing ½<111>(112) edge dislocation with C at O-sites lying along a) TDA(001) and b) TDA(010) and TDA(100).

<100> and <110> Dislocations

The supercell containing <100>{010} dislocation is constructed from the conventional BCC unit cell of Fe with Burgers vector <100> and glide plane {010}, including 115200 Fe atoms. For this edge dislocation, the positions of C at O-sites are symmetric along the Burgers vector <100> and equivalent along TDA(010), TDA(001) and TDA(100), leading to the symmetrical dependence of segregation energy of C with respect to the distance between C and the dislocation core (Fig. 3-16 a). In this dislocation, C is localized in dislocation core area with interaction range about $4\boldsymbol{a}_{\mathbf{Fe}}$ (1.15nm). The lowest segregation energy of C, which is -1.77 eV, is obtained when C locates at the dislocation core. The maximum absolute value of E_{seg} is larger than that in the cases of ½<111> dislocations.

The <100>{011} dislocation with Burgers vector <100> and glide plane (011) which contains 160000 atoms is considered. The segregation energy of C in this dislocation is shown in Fig. 3-16 b. It is found that C atom is localized more strongly in the <100>{011} dislocation core as compared to the one in <100>{010} dislocation, with a segregation energy of 2.00 eV. The interaction range between C and dislocation in the cases of <100> dislocations is around $5\boldsymbol{a}_{\mathbf{Fe}}$ (1.44 nm) which is shorter than that in the cases of ½<111> dislocations.

The supercell of <110>{110} dislcoation, characterzied by <110> Burgers vector {110} glide plane, including 226800 Fe atoms. Here, most unstable dislcoation structure is very complex. Thus, the interaction of C with the most unstable <110>{110} dislocation is studied with C located at dislocation core which is known as the favorable location of C. The lowest segregation energy of -2.57 eV is obtained and shown much lower than in others edge dislocations (Table 3).

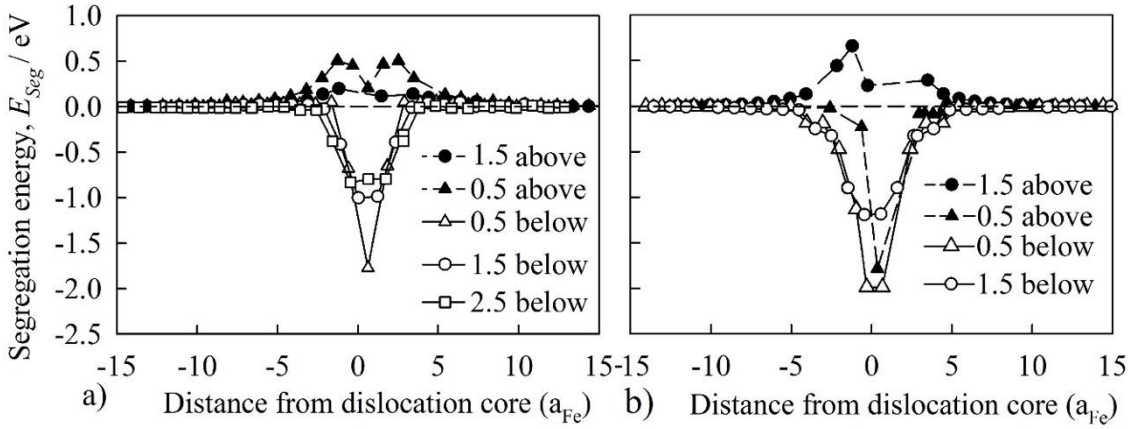

Fig. 3-16. Segregation of C in a) <100>{010} and b) <100>{011} edge dislocations at different layers from the glide plane.

Table 8. Size of simulated supercell containing quadruple edge dislocations, segregation energy (E_{seg}) of C, Voronoi volume (V) around C and shortest Fe-C bond distance (d_{Fe_C}). m is number of Fe atoms in a simulation cell. Here, the supercell size is indicated by using size of basic unit cell of L_x, L_y, L_z.

Configurations	Supercell size $N_1L_x \times N_2L_y \times N_3L_z$			m	Max $\lvert E_{Seg} \rvert$ (eV)	V (Å^3)	$d_{Fe\text{-}C}$ (Å)
	N_1	N_2	N_3				
<111>{110}	120	70	3	151200	1.11	8.00	1. 861
<111>{112}	120	50	5	180000	1.35	8.00	1.924
<100>{010}	120	80	6	115200	1.77	7.67	2.056
<100>{011}	100	80	5	160000	2.00	8.10	1.953
<110>{110}	90	90	5	226800	2.57	8.76	1.963

3.3.4 Local atomic structure and Carbon segregation

To figure out the relation between local atomic structure around C in the dislocation structure and the segregation tendency, the E_{seg} of C for the cases of

½<111>, <100> and <110> dislocations is plotted as a function of Voronoi volume formed by Fe atoms around C atom in Fig. 3-17. It is shown that there is an anti-correlation relation between segregation energy of C and its Voronoi volume. Similar tendency was discovered for the case of grain boundaries.[11)] In Table 3, the E_{seg} of C at the most stable positions in different dislocation configurations and two indicators for the geometry of local atomic structure, namely the Voronoi volume (V) and the shortest Fe-C bond length ($d_{Fe\text{-}C}$). It is found that, in most cases, the most stable segregation site has the largest Voronoi volume and the largest $d_{Fe\text{-}C}$ which was also figured out in the case of grain boundaries. For <100>{010} dislocation, although the $d_{Fe\text{-}C}$ are much longer than the one in other dislocation cases, the interaction of C is weaker than in <100>{011} and <110>{011} edge dislocations. It can be explained that the distances of Fe and C are slightly longer than the equilibrium Fe-C bond length which lead to the weak interaction of Fe and C, similar to the case of grain boudaries.[9,11)] Here, equilibrium Fe-C bond length is the shortest bond lengh of Fe and C in O-site in BCC Fe (1.790Å). Besides, in addition to the Voronoi volume and the shortest Fe-C bond length, the shape of the Voronoi volume formed by neighbour Fe atoms might contribute to the strength of Fe-C interaction.

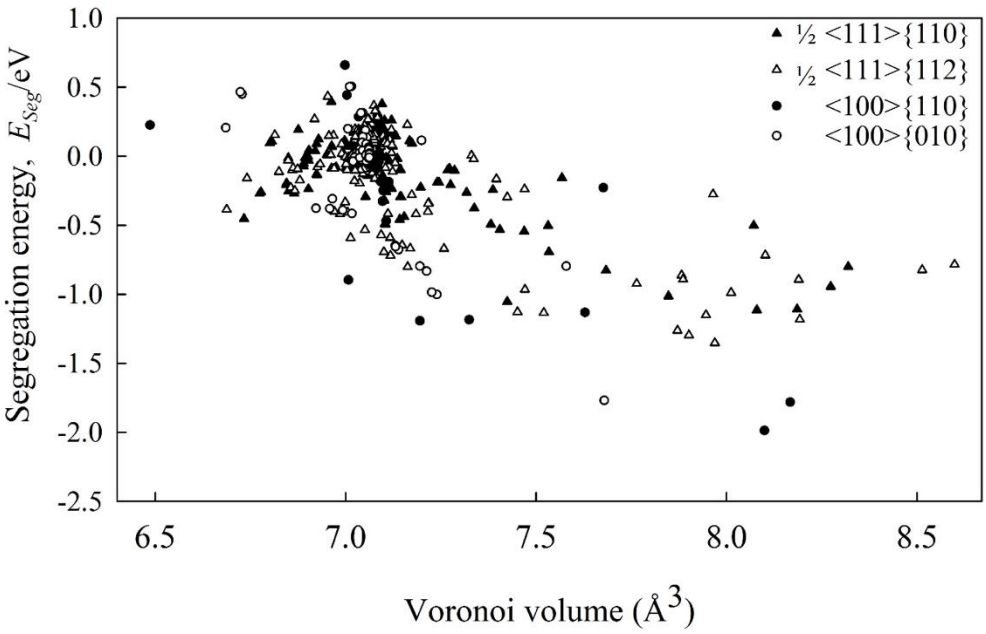

Fig. 3-17. The relationship between segregation energy and Voronoi volume of C in different edge dislocations. In this plot C locates in different layers from the dislocation cores.

3.3.5 Compasion with other defects

In order to compare the strength of interactions between C and defects, the segregation energy of C with different kinds of defect structures is summarized in Fig. 10. In the figure, not only the present results of the E_{seg} of the dislocations systems but also the previous results[11)] on the E_{seg} of grain boundaries and single Fe vacancy are also summarized. As compared to the single vacancy case, the E_{seg} of C in the cases of STGBs and dislocations are more negative, namely, the later defects are more attractive to C than the vacancy. This order is partly consistent with previous DFT calculation of segregation energy of C in bulk Fe with a single vacancy (-0.44 eV), stable ∑3(112) STGB (-0.67 eV).[41,42)] The strongest interaction of C with GB is found to be $-1.78\ eV$ for the unstable GB ∑9(221), which is lower than the one in ½<111> edge dislocations. The interaction of C with the stable dislocations ½<111> is weaker than the unstable <100> and <110> dislocations. The interaction of C with the unstable

dislocations is stronger than the most unstable ∑9(221) STGBs, in contrast to the stable 1/2<111> dislocation. The interaction range of C and grain boundaries (0.8nm) is much shorter than in dislocations (2.89nm).[11] It is known that the segregation energy is related to the solubility of C in Fe matrix. Therefore, it can be concluded that the higher solubility can be obtained by BCC Fe matrix which contains unstable STGBs and dislocations structures. [43] The obtained results might provide useful instruction for experimental studies for controlling the solubility of C through manipulating different defects.

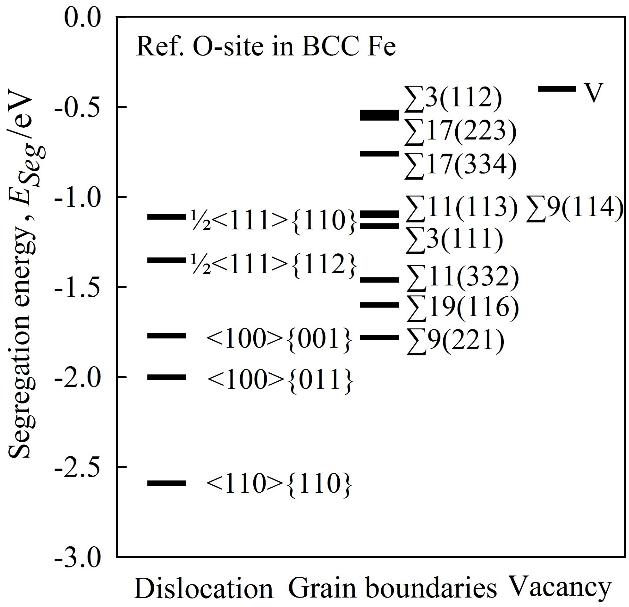

Fig. 3-18 .Energy diagram of C in BCC Fe containing different defects.

CHAPTER 4. CONCLUSION

In this thesis, we have investigated the carbon segregation in three different types of defect structures in α-Fe, namely, point defect, grain boundary and edge dislocation. We have performed large scale atomistic simulations based on newly constructed Tersoff/ZBL interatomic potential, which in turn developed by fitting to the energy and force data from DFT calculations.

In the case of point defect, we focus on a single Fe vacancy and found the most stable position of C is the first nearest neighbour O-site to the vacancy site. The attractive interaction might be due to the open space created by the introduction of athe vacancy. The interaction range between C and vacancy is estimated to be about 5Å.

For the case of symmetrical tilt grain boundaries (STGBs), we have studied the stability of various STGBs and the interaction between STGBs and C. We focus on a series of α-Fe<110> STGBs. Firstly, we found that the Tersoff/ZBL potential works well even for the large complex systems of STGB and can reproduce the energy of STGB reasonably well compared to DFT calculations and previous simulations with using the other interactomic potentials. The stable location of C was also analyzed from the view point of free volume formed by the GB systems. We found that the compact GBs were are less attractive to C than the open ones. The GBs exhibit a strong attractive interaction with C compared to vacancies, therefore, a higher solubility of C can be expected in more open GB systems. The GB is shown to have a short-range interaction with C and this iteraction range is about 10 Å.

For the case of dislocations, we firstly estimated the stability of different dislocation configurations by molecular static calculations. It is confirmed that the dislocation with Burgers vector <111> is the most stable one, which is

consistent with statements in literatures. The interaction between dislocation and C is also explored by calculating segregation energy as in case of grain boundary. In general, C interacts more strongly with the dislocation core compared to the vacancies and the stable grain boundaries. Moreover, it is found that the edge dislocations cause very long-range interaction with C. The interaction range reaches up to about 29Å, which is much longer than the one in case of grain boundary and vacancy.

In order to understand the origin of the interaction between C and defects, we performed Voronoi analysis. Voronoi volumes around C are calculated for various defects and various distance from defects. It is found that the geometry of defect structure is very important to determine the defect and its interaction with C. We found that C is more preferred to be located at the positions which have larger free space, shorter bond length and higher coordination number.

We conclude the segregation difference of considered defects in this thesis. The segregation energy of C in <100>edge dislocations are most negative indicating that C is strongest trapped in these defects. Among calculated defects, point defect vacancy is weakest interaction with C. In dislocation and unstable Σ9(221)GB, C is strongly localized. Comparing to bulk vacancy and Σ3(112)GB and C interaction is stronger. However, C tends to move out of Fe matrix provied by obtainded positive dissolution energies in those defects. Thus, in the Fe matrix which contains various defects, the C will prioritize segregating and locating at diferent defects following the order <100> dislocation > unstable STGB> <111> dislocation > stable STGB > vacancy.

REFERENCES

1. Yang, Z. *et al*. *Comput. Mater. Sci.* **151**, 278–287 (2018).

2. Honeycombe, H. K. D. H. B. and R. W. K. *Steels: microstructure and properties*. (Butterworth-Heinemann, Amsterdam,).

3. Barella, S. *et al*. *Metall. Ital.* **106**, 31–39 (2014).

4. Hristova, E., Janisch, R., Drautz, R., Hartmaier, A. *Comput. Mater. Sci.* **50**, 1088–1096 (2011).

5. Hosford, W. *Tempering and Surface Hardening. In Physical Metallurgy*. (2013).

6. Krauss, G. *Steels: Heat treatment and processing principles*. (1990).

7. Araki, S. *et al*. *Tetsu-to-Hagane* **103**, 491–497 (2017).

8. Liu, Y. L., Zhou, H. B., Zhang, Y., Lu, G. H. & Luo, G. N. *Comput. Mater. Sci.* **50**, 3213–3217 (2011).

9. Ohtsuka, H. *et al*. *ISIJ Int.* **55**, 2483–2491 (2015).

10. Domain, C., Becquart, C. S. & Foct, J. *Phys. Rev. B* **69**, 144112 (2004).

11. Fukai, Y. & Akuma, N. *Phys. Rev. Lett.* **73**, 1640–1643 (1994).

12. Fu, C. C., Meslin, E., Barbu, A., Willaime, F. & Oison, V. *Solid State Phenom.* **139**, 157–164 (2008).

13. Tapasa, K., Barashev, A. V., Bacon, D. J. & Osetsky, Y. N. *Acta Mater.* **55**, 1–11 (2007).

14. Simonetti, S., Juan, A. & Brizuela, G. *Mater. Sci. Pol.* **25**, 885–898 (2007).

15. Rosato, V. *Acta Metall.* **37**, 2759–2763 (1989).

16. Wagenblastt, H., *et al. J. Phys. Chem. Solids Pergamon Press* **23** (1962).

17. Bosman, A. J., Physica, X., Brommer, P. E. Rathenau. *Physica* **23**, 1001-1006 (1957).

18. Kim, S. M., Jackman, J. A., Buyers, W. J. L. & Peterson, D. T. *J. Phys. F Met. Phys.* **14**, 2323–2328 (1984).

19. Lejček, P. Grain Boundaries: Description, Structure and Thermodynamics. in *Springer Series in Materials Science* vol. **136** 5–24 (Springer Verlag, 2010).

20. Literati, C., Mishin, Y. & Wiley, J. *Fundamentals of Grain and Interphase Boundary Diffusion Third, Revised and Enlarged Edition Inderjeet Kaur*.

21. Wolf, D. *Philos. Mag. A Phys. Condens. Matter, Struct. Defects Mech. Prop.* **62**, 447–464 (1990).

22. Krasko, G. L. & Olson, G. B. *Solid State Commun.* **79**, 113–117 (1991).

23. Wu, R., Freeman, A. J. & Olson, G. B. *Phys. Rev. B* **50**, 75–81 (1994).

24. Suzuki, S., Tanii, S., Abiko, K. & Kimura, H. *Metall. Trans. A* **18**, 1109–1115 (1987).

25. Jiang, H. & Szlufarska, I. *Sci. Rep.* **8**, 3736 (2018).

26. Miller, M. K., Beaven, P. A., Brenner, S. S. & Smith, G. D. W. *Metall. Trans. A* **14**, 1021–1024 (1983).

27. de Gruyter, C. B., Verduijn, J. P., Koo, J. Y., Rice, S. B. & Treacy, M. M. J L. *Ultramicroscopy* **34**, 102–107 (1990).

28. Palanisamy, D., Raabe, D. & Gault, B. *Acta Mater.* **174**, 227–236 (2019).

29. Herbig, M. *et al*. *Phys. Rev. Lett.* **112**, 1–5 (2013).

30. Nakashima, H. & Takeuchi, M. 鉄と鋼 **86**, 357--362 (2000).

31. Terentyev, D., He, X., Serra, A. & Kuriplach, J. *Comput. Mater. Sci.* **49**, 419–429 (2010).

32. Wang, J., Janisch, R., Madsen, G. K. H. & Drautz, R. *Acta Mater.* **115**, 259–268 (2016).

33. He, X. *et al*. *Energy Procedia* vol. 127 377–386 (Elsevier Ltd, 2017).

34. Wachowicz, E. & Kiejna, A. *Model. Simul. Mater. Sci. Eng.* **19**, 25001–25021 (2011).

35. Lu, K. *et al*. *J. Phys. Chem. C* **122**, 23191–23199 (2018).

36. Ono, Y. *et al*. *ISIJ Int.* **57**, 1273–1281 (2017).

37. Takebayashl, S., Kunieda, T., Yoshinaga, N., Ushioda, K. & Ogata, S. *ISIJ Int.* **50**, 875–882 (2010).

38. Bertsch, K. M., Meric de Bellefon, G., Kuehl, B. & Thoma, D. J. *Acta Mater*. **199**, 19–33 (2020).

39. Majd, Z. G., Taghizadeh, S. F., Amiri, P. & Vaseghi, B. *J. Magn. Magn. Mater*. **481**, 129–135 (2019).

40. Weinberger, C. R., Boyce, B. L. & Battaile, C. C. *Int. Mater. Rev.* **58**, 296–314 (2013).

41. Khater, H. A., Monnet, G., Terentyev, D. & Serra, A. *Int. J. Plast.* **62**, 34–49 (2014).

42. Simonetti, S., Pronsato, M. E., Brizuela, G. & Juan, A. *Appl. Surf. Sci.* **217**, 56–67 (2003).

43. Wainwright, B. J. A. and T. E. *J. Chem. Phys. 27 1208*.

44. B. J. Alder and T. E. Wainwright, J. Chem. Phys. 31 (1959) 459.

45. R. Car and M. Parrinello, Phys. Rev. Lett. 55 (1985) 2471.

46. Daw, M. S. & Baskes, M. I. *Phys. Rev. B* **29**, 6443–6453 (1984).

47. Mendelev, M. I. *et al*. *Philos. Mag.* **83**, 3977–3994 (2003).

48. Tersoff', J. *Physical Review B* vol. 39.

49. Nguyen, T. Q., Sato, K. & Shibutani, Y. *Mater. Trans.* **59**, (2018) 870

50. Nguyen, T. Q., Sato, K. & Shibutani, Y. Comput. Mater. Sci. **150** (2018) 510

51. Henriksson, K. O. E. & Nordlund, K. Phys. Rev. B **79**, 144107 (2009).

52. Albe, K., Nordlund, K. & Averback, R. S. Phys. Rev. B **65**, 195124 (2002).

53. Ziegler, J. F. & Biersack, J. P. The Stopping and Range of Ions in Matter. in *Treatise on Heavy-Ion Science* 93–129 (Springer US, 1985). doi:10.1007/978-1-4615-8103-1_3.

54. Rycroft, C. H. VORO++: A three-dimensional Voronoi cell library in C++. *Chaos* **19**, 1–16 (2009).

55. S. Plimpton: J. Comp. Phys. **117** (1995) 1

56. Fu, C. C., Torre, J. D., Willaime, F., Bocquet, J. L. & Barbu, A. *Nature Materials* vol. 4 68–74 (2005).

57. Ohnuma, T., Soneda, N. & Iwasawa, M. *Acta Mater.* **57**, 5947–5955 (2009).

58. Ogawa, H. *Mater. Trans.* **47**, 2706–2710 (2006).

59. Kresse, G. & Furthmüller, J. *Phys. Rev. B - Condens. Matter Mater. Phys.*

54, 11169–11186 (1996).

60. Perdew, J. P., Burke, K. & Ernzerhof, M. *Phys. Rev. Lett.* **77**, 3865–3868 (1996).

61. Blöchl, P. E. *Phys. Rev. B* **50**, 17953–17979 (1994).

62. Wachowicz, E., Ossowski, T. & Kiejna, A. *Condens. Matter Mater. Phys.* **81**, 094104 (2010).

63. P. Hirel: Comput. Phys. Commun. 197 (2015) 212219.

64. Tapasa, K., Osetsky, Y. N. & Bacon, D. J. *Acta Mater.* **55**, 93–104 (2007).

65. W. Cai and W. D. Nix: *Imperfections in Crystalline Solids* (Cambridge University Press, 2016)

66. D. J. Dingley and K. F. Hale: Proc. R. Soc. Lond. A **295** (1966) 55

67. D. Hull and D. J. Bacon: *Introduction to Dislocations* (Elsevier, 2011)

67. D. Terentyev, P. Grammatikopoulos, D. J. Bacon and Y. N. Osetsky: Acta Mater. **56** (2008) 5034

68. X. Wang, N. Gao, Y. Wang, H. Liu, G. Shu, C. Li, B. Xu and W. Liu: J. Nucl. Mater. **519** (2019) 322

69. K. Arakawa, M. Hatanaka, E. Kuramoto, K. Ono and H. Mori: Phys. Rev. Lett. 96 (2006) 125506

70. J. A. Yan, C. Y. Wang, W.H. Duan, and S. Y. Wang: Phys. Rev. B **69** (2004) 214110

71. L. S. I. Liyanage, S. G. Kim, J. Houze, S. Kim, M.A. Tschopp, M.I. Baskes, and M.F. Horstemeyer: Phys. Rev. B **89(9)** (2014) 094102

72. D.J. Hepburn, and G.J. Ackland: Phys. Rev. B **78(16)** (2008) 165115

73. T. D. Pham, T. Q. Nguyen, T. Terai, Y. Shibutani, M. Sugiyama and K. Sato: Mater. Trans. **62** (2021) 1057

74. J. Wang, R. Janisch, G. K. H. Madsen and R. Drautz: Acta Mater. **115** (2016) 259

75. C. Domain, C. S. Becquart and J. Foct: Phys. Rev. B **69** (2004) 144112

76. R. Matsumoto, M. Riku, S. Taketomi and N. Miyazaki: Prog. Nucl. Sci. Technol. **2** (2011) 9

PUBLICATIONS

1. **T. D. Pham**, T. Q. Nguyen, T. Terai, Y. Shibutani, M. Sugiyama, and K. Sato**.** Interaction between Carbon and Extended Defects in Fe Studied by First-Principles Based Interatomic Potential. ***Matt. Trans.***, 2022 (acepted)

2. **T. D. Pham**, T. Q. Nguyen, T. Terai, Y. Shibutani, M. Sugiyama, and K. Sato. Segregation of Carbon in α-Fe Symmetrical Tilt Grain Boundaries Studied by First-Principles Based Interatomic Potential**.** ***Matt. Trans.***, 2021, **62**, 1057-1063.

3. T. N.Tran, V. A. Dinh, N. V. Ly, H. D Luong, **T. D. Pham**, T. T. Truong, H. Q. Nguyen, Q. D. Dao, C. T. K. Tran, H. T. T. Bui, D. T. Nguyen, M. N. Ha Dang, V. V T. Phan, and Q. D. T. Novel (110) Double-Layered Guanidinium-Lead Iodide Perovskite Material: Crystal Structure, Electronic Structure, and Broad Luminescence. ***J . Phys. Chem. C,*** 2021, **125**, 1, 964–972.

4. **T. D. Pham**, H. D. Luong, K. Sato, Y. Shibutani and V. A. Dinh. Two-dimensional Na_xSiS as a promising anode material for rechargeable sodium-based batteries: *ab initio* material design. ***Phys. Chem. Chem. Phys.***, 2019, **21**, 24326-24332.

CONFERENCES

1. **T. D. Pham**, T. Q. Nguyen, T. Terai, M. Sugiyama, and K. Sato, *JIM***,** March 2021, Japan.

2. **T. D. Pham**, T. Q. Nguyen, Y. Shibutani, and K. Sato, *PCoMS Symposium*, 2019, Japan.

3. **T. D. Pham**, H. D. Luong, K. Sato, Y. Shibutani and V. A. Dinh, The 9th International Conference on Multiscale Mater. Modeling (MMM2018), 2018, Japan

4. **T. D. Pham**, H. D. Luong, and V. A. Dinh, *ACCMS-Theme Meeting on "Multiscale Modelling of Materials for Sustainable Development*, 2018, Vietnam.